NAVAL POSTGRADUATE SCHOOL

MONTEREY, CALIFORNIA

THESIS

MODELING AND CONTROL OF A MICROGRID USING A HYBRID ENERGY STORAGE SYSTEM WITH SUPERCAPACITORS

by

Michael J. Ross Jr.

June 2018

Thesis Advisor: Giovanna Oriti
Co-Advisor: Roberto Cristi

Approved for public release. Distribution is unlimited.

THIS PAGE INTENTIONALLY LEFT BLANK

REPORT DOCUMENTATION PAGE			*Form Approved OMB No. 0704-0188*

1. AGENCY USE ONLY *(Leave blank)*	**2. REPORT DATE** June 2018	**3. REPORT TYPE AND DATES COVERED** Master's thesis

4. TITLE AND SUBTITLE MODELING AND CONTROL OF A MICROGRID USING A HYBRID ENERGY STORAGE SYSTEM WITH SUPERCAPACITORS	**5. FUNDING NUMBERS**
6. AUTHOR(S) Michael J. Ross Jr.	
7. PERFORMING ORGANIZATION NAME(S) AND ADDRESS(ES) Naval Postgraduate School Monterey, CA 93943-5000	**8. PERFORMING ORGANIZATION REPORT NUMBER**
9. SPONSORING / MONITORING AGENCY NAME(S) AND ADDRESS(ES) N/A	**10. SPONSORING / MONITORING AGENCY REPORT NUMBER**

11. SUPPLEMENTARY NOTES The views expressed in this thesis are those of the author and do not reflect the official policy or position of the Department of Defense or the U.S. Government.

12a. DISTRIBUTION / AVAILABILITY STATEMENT Approved for public release. Distribution is unlimited.	**12b. DISTRIBUTION CODE** A

13. ABSTRACT (maximum 200 words)

Lead-acid batteries have traditionally been used for energy storage in microgrid applications. Implementing an Energy Management System (EMS)-controlled supercapacitor (SC) and lead-acid battery hybrid energy storage system (HESS) has been shown to reduce operational costs by extending battery lifetimes. The SCs can be controlled to provide the high-frequency, power-dense component of the load power, which reduces the daily cyclical stress and state-of-charge (SOC) depletion of the lead-acid batteries; however, the HESS must be appropriately sized based on cost constraints, available power sources, and load demand.

The enabling theory and design of a SIMULINK model of a DC microgrid are discussed in this thesis. The results obtained from this model illustrate the energy exchange between microgrid components, demonstrate some of the potential benefits of implementing a HESS, and provide useful data for battery and SC sizing. The DC microgrid model is scalable and can use any user-defined combination of source and load profiles. In islanded mode, the lead-acid battery and SC banks need to be unrealistically large to provide adequate power to the load. In grid-connected mode, the HESS sizing requirements are significantly reduced, and the overall energy savings of the system are improved.

14. SUBJECT TERMS Energy Management System (EMS), hybrid energy storage system (HESS), lead-acid battery, supercapacitor (SC), microgrid	**15. NUMBER OF PAGES** 79
	16. PRICE CODE

17. SECURITY CLASSIFICATION OF REPORT	**18. SECURITY CLASSIFICATION OF THIS PAGE**	**19. SECURITY CLASSIFICATION OF ABSTRACT**	**20. LIMITATION OF ABSTRACT**
Unclassified	Unclassified	Unclassified	UU

NSN 7540-01-280-5500 Standard Form 298 (Rev. 2-89) Prescribed by ANSI Std. 239-18

THIS PAGE INTENTIONALLY LEFT BLANK

Approved for public release. Distribution is unlimited.

MODELING AND CONTROL OF A MICROGRID USING A HYBRID ENERGY STORAGE SYSTEM WITH SUPERCAPACITORS

Michael J. Ross Jr.
Ensign, United States Navy
BS, United States Naval Academy, 2017

Submitted in partial fulfillment of the
requirements for the degree of

MASTER OF SCIENCE IN ELECTRICAL ENGINEERING

from the

NAVAL POSTGRADUATE SCHOOL
June 2018

Approved by: Giovanna Oriti
Advisor

Roberto Cristi
Co-Advisor

R. Clark Robertson
Chair, Department of Electrical and Computer Engineering

THIS PAGE INTENTIONALLY LEFT BLANK

ABSTRACT

Lead-acid batteries have traditionally been used for energy storage in microgrid applications. Implementing an Energy Management System (EMS)-controlled supercapacitor (SC) and lead-acid battery hybrid energy storage system (HESS) has been shown to reduce operational costs by extending battery lifetimes. The SCs can be controlled to provide the high-frequency, power-dense component of the load power, which reduces the daily cyclical stress and state-of-charge (SOC) depletion of the lead-acid batteries; however, the HESS must be appropriately sized based on cost constraints, available power sources, and load demand.

The enabling theory and design of a SIMULINK model of a DC microgrid are discussed in this thesis. The results obtained from this model illustrate the energy exchange between microgrid components, demonstrate some of the potential benefits of implementing a HESS, and provide useful data for battery and SC sizing. The DC microgrid model is scalable and can use any user-defined combination of source and load profiles. In islanded mode, the lead-acid battery and SC banks need to be unrealistically large to provide adequate power to the load. In grid-connected mode, the HESS sizing requirements are significantly reduced, and the overall energy savings of the system are improved.

THIS PAGE INTENTIONALLY LEFT BLANK

TABLE OF CONTENTS

LIST OF FIGURES

LIST OF TABLES

THIS PAGE INTENTIONALLY LEFT BLANK

LIST OF ACRONYMS AND ABBREVIATIONS

BBC	buck-boost converter
CNIC	Commander, Navy Installations Command
CNO	Chief of Naval Operations
DER	distributed energy resource
DOD	depth-of-discharge
DoN	Department of the Navy
EMS	energy management system
FOB	forward operating base
HESS	hybrid energy storage system
HPF	high pass filter
KCL	Kirchhoff's current law
KVL	Kirchhoff's voltage law
LPF	low pass filter
LUT	lookup table
OPNAV	Office of the Chief of Naval Operations
PI	proportional-integral
PV	photovoltaic
SC	supercapacitor
SOC	state-of-charge
TOU	time-of-use

THIS PAGE INTENTIONALLY LEFT BLANK

ACKNOWLEDGMENTS

This thesis effort would not have been possible without the help of Professors Giovanna Oriti and Roberto Cristi. They invested considerable time and effort into guiding me during this process and never hesitated to make time in their busy schedules to meet with me. It was a pleasure to work with them, and I could always tell that they truly cared about the development of their students and advisees.

I also would like to acknowledge all of the professors and teachers that I have had the fortune to work with in the past. They gave me the academic foundation I needed to understand the science that enables the technology described in my thesis. Professors Brian Jenkins and Charles Nelson at the United States Naval Academy spent a significant amount of time proofreading my research papers as an undergraduate and helping me grow as a technical writer. CDR John Stevens, USN, encouraged me to attend the Naval Postgraduate School and to pursue the power engineering track.

Finally, I would like to thank my family. Both of my grandfathers inspired me to pursue a military career, and my parents have supported me directly during my time in the Navy. My brother and sister are constant sources of motivation.

THIS PAGE INTENTIONALLY LEFT BLANK

I. INTRODUCTION

In this chapter, the operational needs, programs, and statistics that motivate this research are introduced. Findings from previous experiments as well as the problems, objectives, and potential benefits of this thesis effort are then briefly explained.

A. MOTIVATION

There is a growing need for secure and efficient production, storage, and distribution of electrical energy at Navy installations. According to Commander, Navy Installations Command (CNIC), energy bills account for approximately 28% of the Navy's shore budget, making them the "single largest cost for Navy installations" [1]. In order to continue accomplishing its increasingly complex missions with a shrinking budget, the Department of the Navy (DoN) created the Marine Corps Expeditionary Energy Program in 2009 and the Navy Shore Energy Program in 2010. Secretary of the Navy Ray Mabus set several goals for the DoN in 2009, including a 50% reduction in petroleum use in the commercial fleet by 2015 and for 50% of the DoN's energy consumption (both ashore and afloat) to come from alternative sources by 2020 [2]. The Chief of Naval Operations (CNO) promulgated Office of the Chief of Naval Operations (OPNAV) Instruction 4100.5E in 2012 to provide policy for the implementation of these programs and explain the Navy's energy management vision. The guiding principles behind this policy include energy efficiency, renewable energy and sustainability, and Navy culture and behavior [3]. Installing controllable energy storage elements in the local grids at military installations contributes to all three of these objectives by increasing the overall cost-effectiveness of the Navy's energy consumption, improving the effectiveness of intermittent renewable energy sources, and changing the patterns of energy consumption at Navy installations.

B. PURPOSE

In recent studies, power electronics based Energy Management Systems (EMS) have proven to be able to address all of the guiding principles of OPNAVINST 4100.5E in microgrid environments. Microgrids are defined as "intentional islands formed at a customer facility" that have "at least one distributed energy resource (DER) and associated

loads" and can "include parts of the local utility distribution system" [4]. Several DERs have been tested in microgrid applications, including lead-acid batteries [5–14], supercapacitors (SCs) [6–10], [12–18], wind farms [9–12], [16], photovoltaic (PV) cells [11–15], and flywheels [19–23]. When connected to the local utility grid, an EMS-controlled microgrid can reduce energy costs by "shaving" the peak power demanded from the grid, which reduces both demand costs (determined by overall peak power demand) and time-of-use (TOU) costs (highest during "peak" periods, typically from 1200–1800 daily). The EMS can also manage any DERs and energy storage elements connected to the microgrid system. If the microgrid is operating in islanded mode, the EMS can shed noncritical loads as necessary to ensure continuous power to loads that are critical to "safety or mission success" [24].

Lead-acid batteries have been used and studied extensively in energy storage and electric vehicle applications due to their relatively high energy density and efficiency (when compared with other battery types) [25]; however, conventional lead-acid batteries are not designed for sustained deep discharge cycles, which are common in remote microgrid applications [25]. Lead-acid batteries are also expensive to purchase and, in military forward operating base (FOB) environments, dangerous to transport and replace [24]. Hybridizing the energy storage elements in an EMS can improve battery lifetime and reduce long-term replacement costs. Recently, Hybrid Energy Storage Systems (HESSs) with batteries and SCs have been studied in microgrid applications. SCs offer several advantages when compared to batteries, including higher charge and discharge rates [9], [13], [17], much higher cyclical lifetimes (on the order of hundreds of thousands) [9–10], [16–17], light weight [9], low material toxicity [9], high cycle efficiency [9], lower internal resistance [17], deeper discharge capability [17], and higher power density [8], [10], [13], [16]; however, due to their limited terminal voltage, SCs have relatively low-energy density [8] [10], [13], [17]. In a well-designed HESS, the batteries provide the low-frequency, energy-dense component of the load demand, and the SCs provide the high-frequency, power-dense component.

In an EMS-controlled microgrid with battery and SC energy storage, the DC bus that connects the sources and HESS elements to the loads experiences large input current

ripples during load transients. The EMS can be configured to divert higher-order current ripple to the SCs via a high pass filter (HPF) and the low-frequency current demand to the batteries using a low pass filter (LPF) [26]. In this thesis, we focus on modeling the exchange of power and energy between the SCs, batteries, and loads using this filtering configuration. These models improve upon previous work by allowing the user to adjust the responsiveness of the SCs and by providing useful measurements for more efficient battery and SC sizing. Additionally, the battery and SC models more accurately reflect the effects of state-of-charge (SOC), charging and discharging currents, and terminal voltage limitations on battery and SC performance.

C. RESEARCH OBJECTIVES

The primary research objective of this thesis is to model the exchange of electrical energy and power between the source, storage, and load elements in a simulated EMS-controlled microgrid with a battery and SC HESS, a LPF connected to the battery bank, and a HPF connected to the SC bank. Secondary objectives of this thesis include improving the sizing of the SC and battery elements of the HESS and quantifying the overall efficiency of the modeled microgrid system.

D. RELATED WORK

Several recent publications explore the advantages of using a battery and SC HESS over a traditional battery bank in microgrid applications [7–16], [26]. Many power control schemes have been proposed, including proportional-integral (PI) control [6], [9], [11], low pass filtering [8], high pass filtering [10], neural networks [7], model predictive control [7], and multi-objective optimization [15]. The HESS power control method used in this thesis is similar to the approach explained in [14] and [26].

Numerous battery and SC models have been proposed in recent literature, including, but not limited to, series RC circuits [6], parallel RC branches [7], [16], and complex arrangements of components with variable parameters [10]. The battery and SC models used in this thesis are adapted from [10]. These models account for the nonlinear effects of SOC on the internal resistances and capacitance of the lead-acid battery as well as the effects of the terminal voltage on the capacitance of the SC.

The lifetimes of lead-acid batteries are impacted by a variety of factors, including, but not limited to, depth-of-discharge (DOD) [10], cycling [10], temperature [18], and maintenance [24]. Although it is difficult to precisely model all of these effects, the Rainflow counting algorithm is used in [10] and [14] to approximate the increase in lead-acid battery lifetime when a HESS is implemented.

II. BATTERY AND SUPERCAPACITOR THEORY

Before analyzing the performance of batteries and SCs in microgrid applications, it is essential to understand the basic theories that describe the behavior of these hybrid energy storage elements. The necessary background information is provided in this chapter.

A. LEAD-ACID BATTERIES

There are several factors that influence the behavior of a lead-acid battery, including battery temperature, SOC, internal resistances, and current limits [10]. If the battery temperature is maintained at 25°C, the schematic of a single lead-acid battery (shown in Figure 1) simplifies to an ideal voltage source $v_{Bi,1}$ in series with an internal resistance R_B. The relationship between open-circuit voltage v_{Bi} and battery state-of-charge SOC_B (shown in Figure 2) as well as the maximum battery discharge current can be found in the battery data sheets [27].

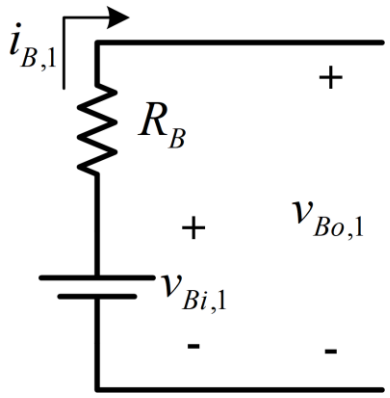

Figure 1. Single Lead-Acid Battery Schematic

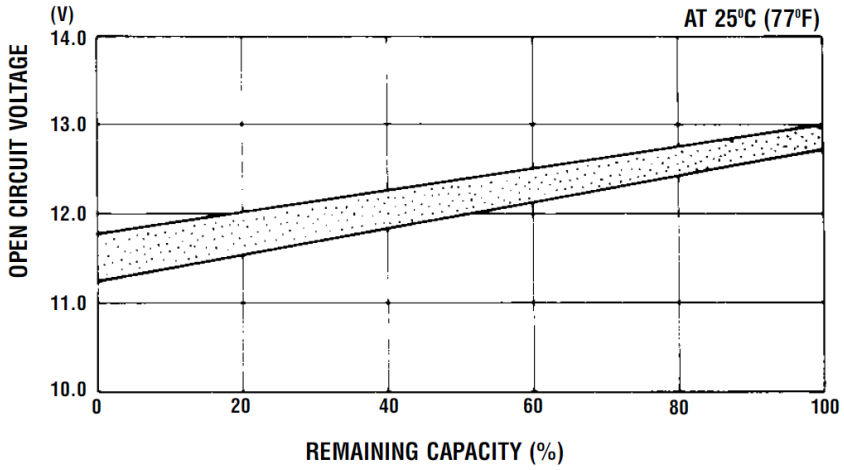

Figure 2. Relationship between v_{Bi} and SOC_B. Source: [27].

Applying Kirchhoff's Voltage Law (KVL) across the closed loop in the circuit shown in Figure 1 gives

$$v_{Bo,1}(t) = v_{Bi,1}(t) - i_{B,1}(t)R_B \ , \tag{1}$$

where $v_{Bo,1}(t)$ is the voltage across the leads of a single battery when outputting the current $i_{B,1}(t)$. Also, applying Watt's Law gives the following expressions for input power $P_{Bi,1}(t)$, resistive loss $P_{BR,1}(t)$, and output power $P_{Bo,1}(t)$, respectively, of a single lead-acid battery:

$$P_{Bi,1}(t) = v_{Bi,1}(t)i_{B,1}(t), \tag{2}$$

$$P_{BR,1}(t) = i_{B,1}^2(t)R_{B,1}, \tag{3}$$

and

$$P_{Bo,1}(t) = v_{Bo,1}(t)i_{B,1}(t) = P_{Bi,1}(t) - P_{BR,1}(t). \tag{4}$$

The state-of-charge in Ampere-seconds (A·s) of a single lead-acid battery $SOC_{B,1}(t)$ is

$$SOC_{B,1}(t) = \frac{3600 \text{ s}}{1 \text{ hour}} SOC_{B,1}(0) - \int_0^t i_{B,1}(\tau)d\tau, \tag{5}$$

where $SOC_{B,1}(0)$ is the initial state-of-charge in Ampere-hours (A·h) and t is the time in seconds.

B. LEAD-ACID BATTERY BANKS

As shown in Figure 3, lead-acid batteries can be arranged in a bank with N_{Bp} parallel branches and N_{Bs} series elements in each branch. The currents in each parallel branch and the voltages in each series element are additive; therefore, increasing N_{Bp} increases the overall A·h capacity of the battery bank and increasing N_{Bs} increases the overall terminal voltage v_{Bo}.

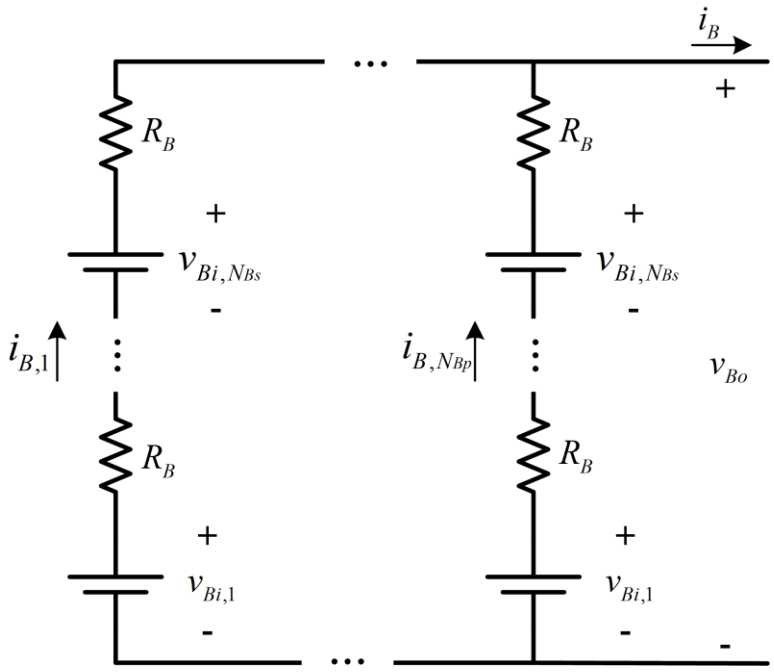

Figure 3. $N_{Bp} \times N_{Bs}$ Lead-Acid Battery Bank Schematic

If all batteries in the bank are identical and are initially fully charged, the current flowing through each parallel branch is $i_B(t)/N_{Bp}$. Applying KVL across one parallel branch gives the battery bank output voltage $v_{Bo}(t)$ as

$$v_{Bo}(t) = N_{Bs}\left(v_{Bi}(t) - R_B\frac{i_B(t)}{N_{Bp}}\right). \tag{6}$$

Applying Watt's Law gives the following expressions for input power $P_{Bi}(t)$, resistive loss $P_{BR}(t)$, and output power $P_{Bo}(t)$, respectively, of a $N_{Bp} \times N_{Bs}$ lead-acid battery bank:

$$P_{Bi}(t) = N_{Bp}\left(N_{Bs} v_{Bi}(t) \frac{i_B(t)}{N_{Bp}} \right) = N_{Bs} v_{Bi}(t) i_B(t), \tag{7}$$

$$P_{BR}(t) = N_{Bp}\left(N_{Bs}\left(\frac{i_B(t)}{N_{Bp}} \right)^2 R_B \right) = \frac{N_{Bs}}{N_{Bp}} {i_B}^2(t) R_B, \tag{8}$$

and

$$P_{Bo}(t) = v_{Bo}(t) i_B(t) = P_{Bi}(t) - P_{BR}(t). \tag{9}$$

If all batteries charge and discharge identically, the state-of-charge $SOC_B(t)$ in A·s of any battery in the $N_{Bp} \times N_{Bs}$ arrangement is

$$SOC_B(t) = \frac{3600 \text{ s}}{1 \text{ hour}} SOC_B(0) - \int_0^t \frac{i_B(\tau)}{N_{Bp}} d\tau \quad . \tag{10}$$

C. SUPERCAPACITORS

When considering SCs in energy storage applications, it is important to first understand the theories and equations that govern the behavior of conventional capacitors. Modeling SC performance requires an understanding of these foundational principles as well as the unique physical and chemical properties of SCs.

1. Conventional (Electrolytic) Capacitors

An electrolytic capacitor is a passive electrical device with a dielectric material placed between two electrodes. Capacitors store energy in the electric field that is created when charges of opposite polarity accumulate on the electrodes. When a voltage V is applied across the electrodes of a capacitor, the charge Q that accumulates on the electrodes is

$$Q = CV, \tag{11}$$

where C is the capacitance. The capacitance of a basic parallel-plate capacitor is

$$C = \varepsilon_r \varepsilon_0 \frac{A}{d}, \tag{12}$$

where ε_r is the relative permittivity (a unitless ratio), ε_0 is the electrical permittivity of free space (8.85×10^{-12} F/m), A is the electrode cross-sectional, and d is the separation between the two plates. The energy E_C stored in the electric field of a capacitor is

$$E_C = \int Q \, dV = \frac{1}{2} C V^2 . \tag{13}$$

2. Supercapacitors

Compared to electrolytic capacitors, SCs (also called ultracapacitors, electric double-layer capacitors, or electrochemical capacitors) can hold a much higher charge at a given voltage because of their chemical composition. SC electrodes are typically covered in porous material (such as graphene or carbon nanotubes [28]), which increases their effective surface area. Also, instead of being separated by a single dielectric layer, SC electrodes are separated by a relatively thin insulator (called the separator) soaked in an electrolyte. As shown in Figure 4, the separator creates layers of opposing charge on both sides of the separator when the electrodes are charged. These physical and chemical properties allow SCs to achieve higher capacitances and power densities than their conventional counterparts.

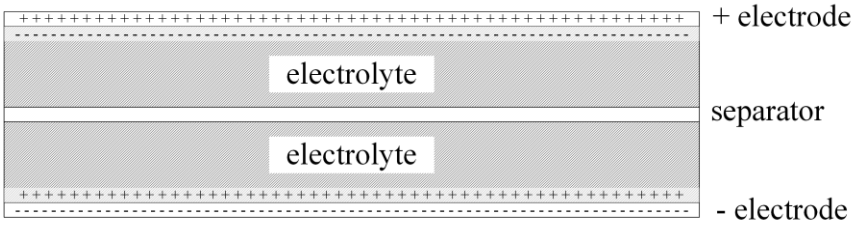

Figure 4. Supercapacitor Physical Architecture

Similarly to lead-acid batteries, SCs are influenced by many factors, including temperature, frequency, SOC, internal resistances, and current limits [26]. If the temperature is maintained at 25°C and the effects of frequency are ignored, the effective schematic of a single SC (shown in Figure 5) simplifies to an ideal capacitance C_{SC} (with voltage $v_{SCi,1}$) and a constant effective series resistance R_{esr}.

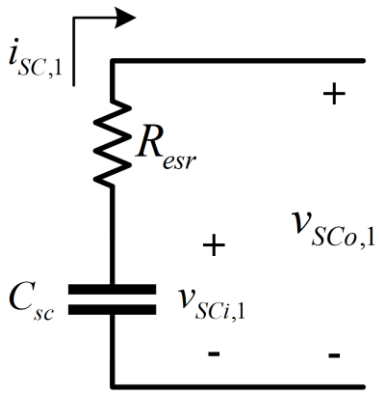

Figure 5. Single Supercapacitor Schematic

The charge and energy stored in a SC are described by (11) and (13), respectively. The energy stored in a single SC with capacitance C_{SC}, or its state-of-charge $SOC_{SC,1}(t)$ in Joules, is given by

$$SOC_{SC,1}(t) = \frac{3600\text{ s}}{1\text{ hour}} SOC_{SC,1}(0) - \int_0^t v_{SCi,1}(\tau) i_{SC,1}(\tau) d\tau\,, \tag{14}$$

where $SOC_{SC,1}(0)$ is the initial state-of-charge in Watt-hours (W·h) and $v_{SCi}(t)$ is the time-varying open-circuit SC voltage, given by

$$v_{SCi,1}(t) = \sqrt{\frac{2SOC_{SC,1}(t)}{C_{SC}}}\,. \tag{15}$$

Applying KVL across the closed loop in the circuit shown in Figure 5 gives

$$v_{SCo,1}(t) = v_{SCi,1}(t) - i_{SC,1}(t) R_{esr}\,, \tag{16}$$

where $v_{SCo,1}(t)$ is the voltage across the leads of a single SC in the presence of current $i_{SC,1}(t)$. Applying Watt's Law gives the following expressions for input power $P_{SCi,1}(t)$, resistive loss $P_{SCR,1}(t)$, and output power $P_{SCo,1}(t)$, respectively, of a single supercapacitor:

$$P_{SCi,1}(t) = v_{SCi,1}(t) i_{SC,1}(t)\,, \tag{17}$$

$$P_{SCR,1}(t) = i_{SC,1}^2(t) R_{esr}\,, \tag{18}$$

and

$$P_{SCo,1}(t) = v_{SCo,1}(t) i_{SC,1}(t) = P_{SCi,1}(t) - P_{SCR,1}(t)\,. \tag{19}$$

D. SUPERCAPACITOR BANKS

As shown in Figure 6, much like lead-acid batteries, SCs can be arranged in a bank with N_{SCp} parallel branches and N_{SCs} series elements in each branch. The currents in each parallel branch and the voltages in each series element are additive; therefore, increasing N_{SCp} increases the overall W·h capacity of the battery bank and increasing N_{SCs} increases the overall terminal voltage v_{SCo}.

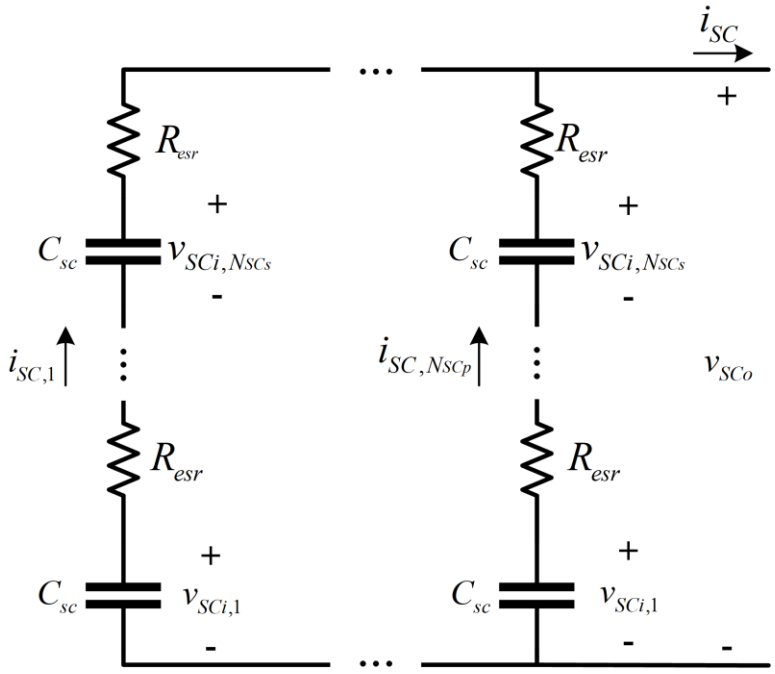

Figure 6. $N_{SCp} \times N_{SCs}$ Supercapacitor Bank Schematic

If all SCs charge and discharge identically, the state-of-charge $SOC_{SC}(t)$ in Joules of any single SC within the $N_{SCp} \times N_{SCs}$ arrangement is

$$SOC_{SC}(t) = \frac{3600 \text{ s}}{1 \text{ hour}} SOC_{SC}(0) - \int_0^t v_{SCi}(\tau) \frac{i_{SC}(\tau)}{N_{SCp}} d\tau \tag{20}$$

The open-circuit voltage of any single SC within the $N_{SCp} \times N_{SCs}$ arrangement is related to $SOC_{SC}(t)$ as

$$v_{SCi}(t) = \sqrt{\frac{2SOC_{SC}(t)}{C_{SC}}} \,. \tag{21}$$

If all SCs in the bank are identical and are initially fully charged, the current flowing through each parallel branch is $i_{SC}(t) / N_{SCp}$. Applying KVL across one parallel branch gives the SC bank output voltage $v_{SCo}(t)$ as

$$v_{SCo}(t) = N_{SCs}\left(v_{SCi}(t) - R_{esr}\frac{i_{SC}(t)}{N_{SCp}} \right) . \tag{22}$$

Applying Watt's Law gives the following expressions for input power $P_{SCi}(t)$, resistive loss $P_{SCR}(t)$, and output power $P_{SCo}(t)$, respectively, of a $N_{SCp} \times N_{SCs}$ SC bank:

$$P_{SCi}(t) = N_{SCp}\left(N_{SCs} v_{SCi}(t)\frac{i_{SC}(t)}{N_{SCp}} \right) = N_{SCs} v_{SCi}(t) i_{SC}(t) , \tag{23}$$

$$P_{SCR}(t) = N_{SCp}\left(N_{SCs}\left(\frac{i_{SC}(t)}{N_{SCp}} \right)^2 R_{esr} \right) = \frac{N_{SCs}}{N_{SCp}} {i_{SC}}^2(t) R_{esr} , \tag{24}$$

and

$$P_{SCo}(t) = v_{SCo}(t) i_{SC}(t) = P_{SCi}(t) - P_{SCR}(t) . \tag{25}$$

III. BATTERY AND SUPERCAPACITOR MODELS

The battery and SC banks were modeled using MATLAB and SIMULINK. The implementation of (6)-(10) and (20)-(25) in these models is described in this chapter. Both models allow for bidirectional current flow, meaning that the components can either be discharged (positive currents) or charged (negative currents) at any time during the simulation.

A. BATTERY MODEL

The $N_{Bp} \times N_{Bs}$ lead-acid battery bank was modeled in SIMULINK using (6)-(10) as well as the data plotted in Figure 2. As shown in Figure 7, the battery bank model has one input (battery current i_B) and four outputs (battery bank terminal voltage v_{Bo}, input power P_{Bi}, resistive losses P_{BR}, and output power P_{Bo}). This subsystem-level model is color coded to illustrate how each equation is implemented and to clarify the sequence of computations that relates the input to the outputs.

The battery bank model parameter values (listed in Table 1) are derived from manufacturer specifications [27]. As a conservative estimate (to account for connection, line, and protection circuit losses), R_B is set to ten times its full-charge specification value. The lookup table (LUT) data were obtained from the average values in the plot shown in Figure 2.

Table 1. Battery Bank Model Parameter Values. Adapted from [27].

Parameter	Symbol	Value	Units
Battery internal resistance	R_B	160	mΩ
Maximum battery SOC	SOC_{Bmax}	12	A·h
Initial battery SOC	$SOC_B(0)$	12	A·h
Maximum battery current	i_{Bmax}	40	A
Battery SOC LUT data	SOC_{Bdata}	0:100	%
Battery voltage LUT data	v_{Bidata}	11.5:0.0136:12.86	V

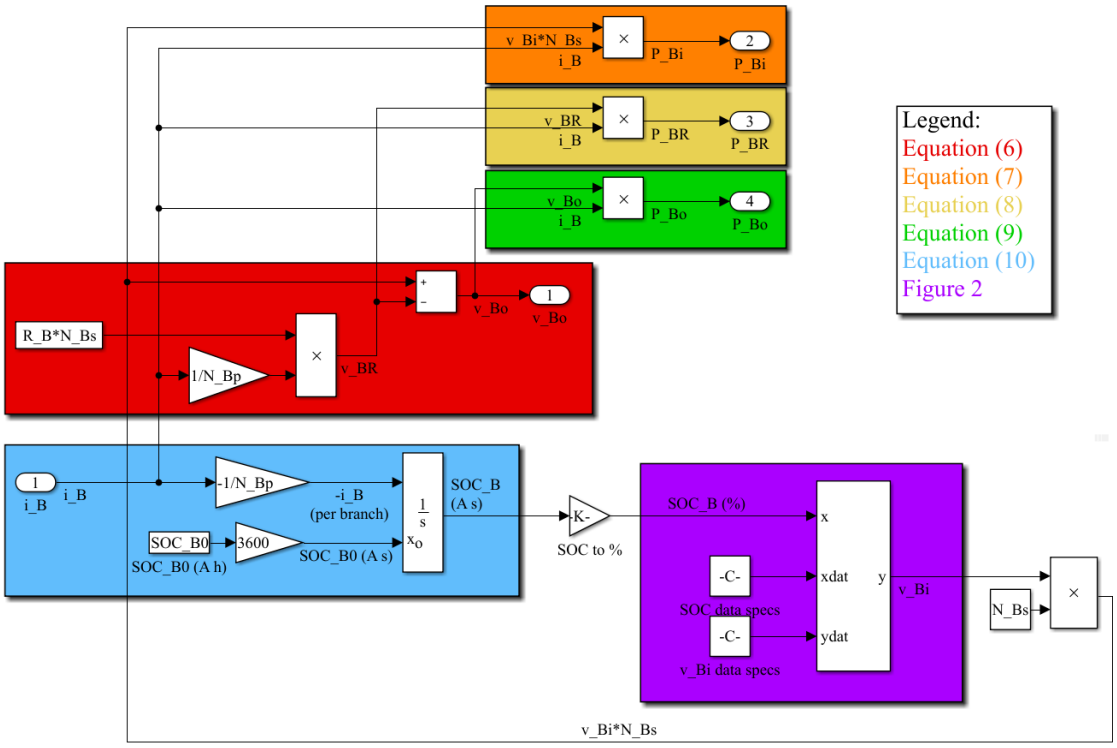

Figure 7. Lead-Acid Battery Bank SIMULINK Model

B. SUPERCAPACITOR MODEL

The $N_{SCp} \times N_{SCs}$ SC bank was modeled in SIMULINK using (20)-(25). As shown in Figure 8, like the battery bank model, the SC bank model has one input (SC current i_{SC}) and four outputs (SC bank terminal voltage v_{SCo}, input power P_{SCi}, resistive losses P_{SCR}, and output power P_{SCo}). This subsystem-level model is color coded to illustrate how each equation is implemented and to clarify the sequence of computations that relates the input to the outputs.

Instead of using a LUT and previously collected data to interpolate an open-circuit voltage value (as is done in the battery bank model), the SC bank model uses (21) to calculate the open-circuit voltage using the remaining energy left on each SC (initially set to 100% charge, or 57 W·h). The calculated value of v_{SCi} is then multiplied by the SC

current in each parallel branch to calculate the instantaneous input power generated by each SC, which is integrated as done in (20).

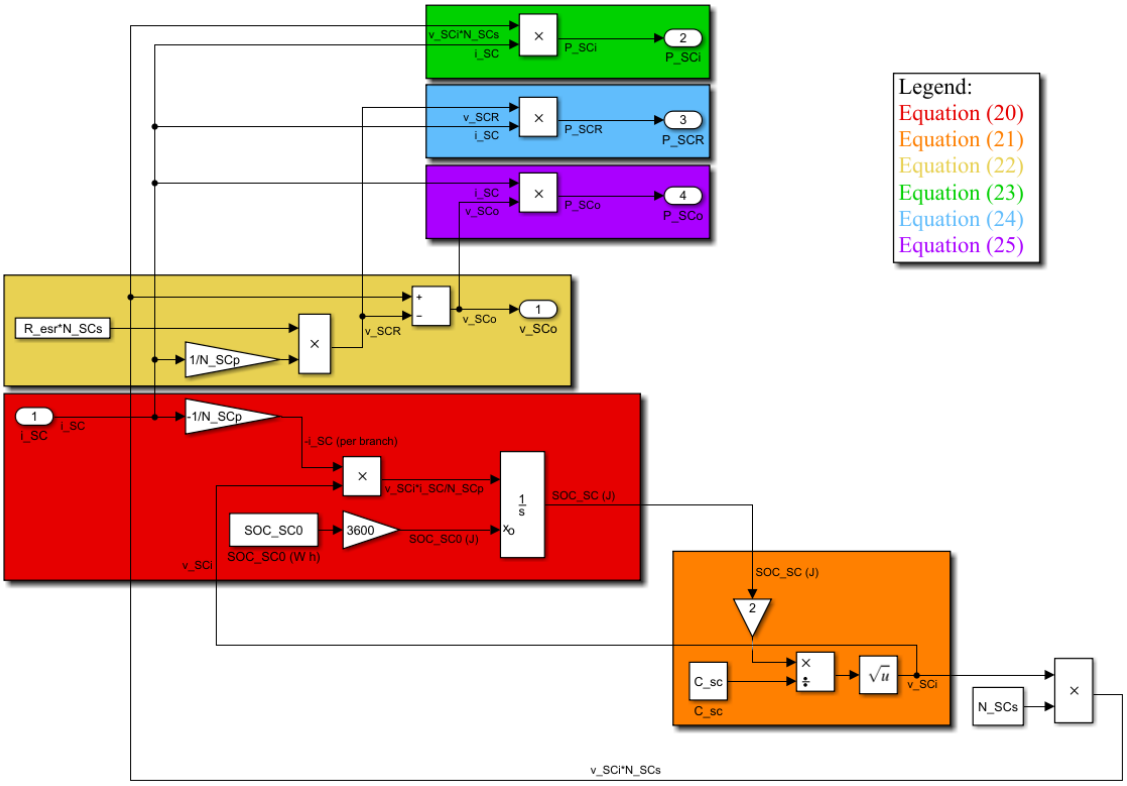

Figure 8. Supercapacitor Bank SIMULINK Model

The SC bank model parameter values (listed in Table 2) are derived from manufacturer specifications [29].

Table 2. Supercapacitor Bank Model Parameter Values. Adapted from [29].

Parameter	Symbol	Value	Units
SC capacitance	C_{SC}	130	F
Equivalent series resistance	R_{esr}	8.1	mΩ
Maximum SC SOC	SOC_{SCmax}	57	W·h
Initial SC SOC	$SOC_{SC}(0)$	57	W·h
Maximum SC current	$i_{SC\,max}$	1900	A

THIS PAGE INTENTIONALLY LEFT BLANK

IV. ISLANDED DC MICROGRID SIMULATION

The battery and SC models are implemented within a larger islanded DC microgrid model that simulates a 24-hour load profile sourced by HESS elements and PV panels. The system components, SIMULINK model, control scheme, HESS sizing procedure, and simulation results are explained in this chapter.

A. SYSTEM COMPONENTS

A block diagram of the islanded DC microgrid model is shown in Figure 9. In the context of this thesis, an "islanded" microgrid is disconnected from the local utility grid, and its loads are completely sourced by renewable sources and HESS elements.

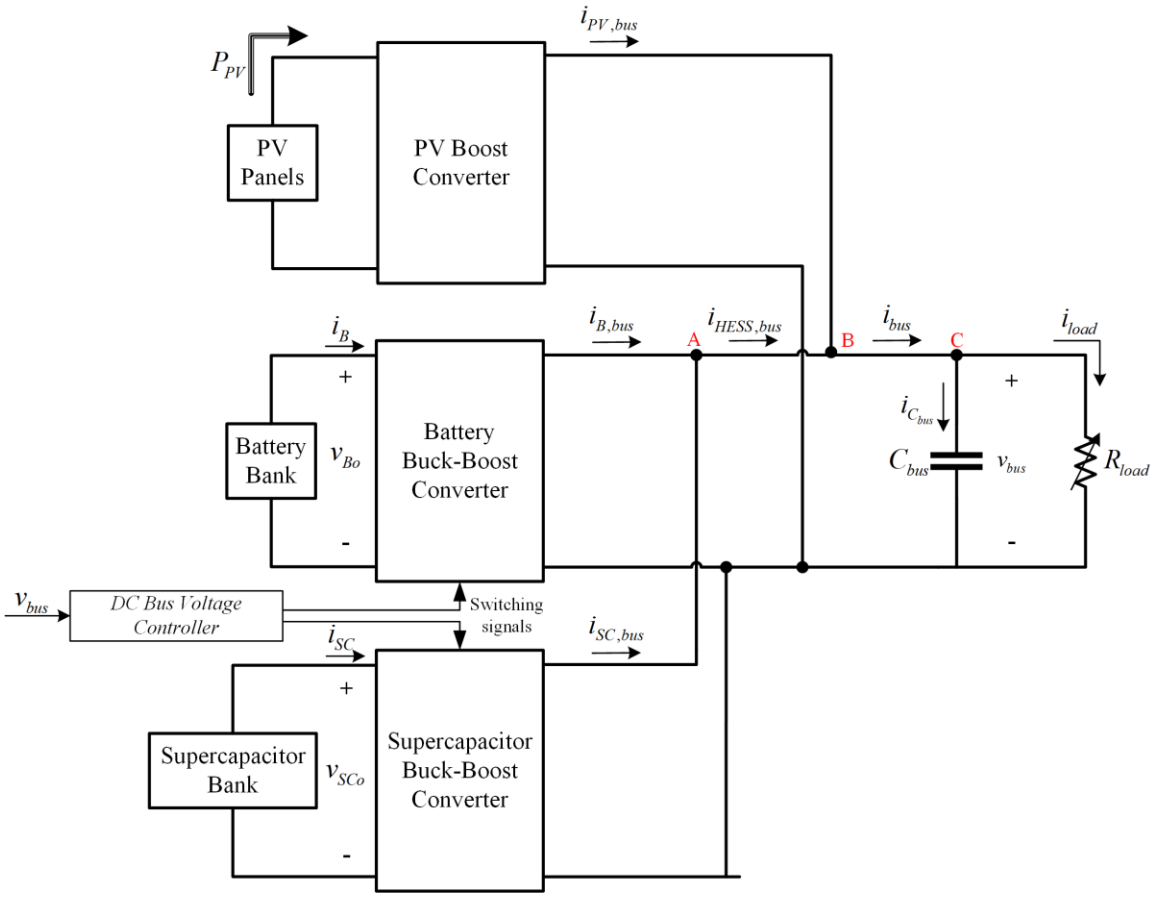

Figure 9. Islanded DC Microgrid Block Diagram

1. Bi-directional Buck-Boost Converters

Bi-directional buck-boost converters (BBCs) are used in this model to allow power to flow in either direction between the HESS elements and the load and to allow the battery and supercapacitor banks to operate at different voltages from the DC bus [26]. As shown in Figures 10 and 11, when the boost switch is modulated and the buck switch remains open, the BBC operates in boost mode and the source discharges energy to the load. Conversely, when the buck switch is modulated and the boost switch remains open, the BBC operates in buck mode and the source is being charged.

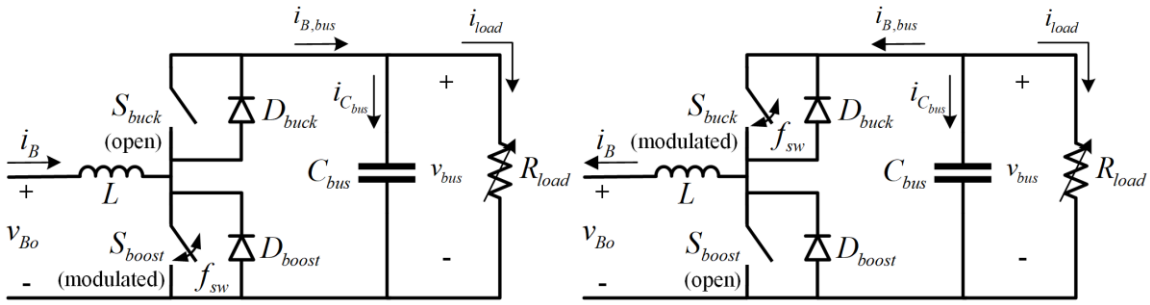

Figure 10. Battery BBC Operation (Left: Boost Mode; Right: Buck Mode)

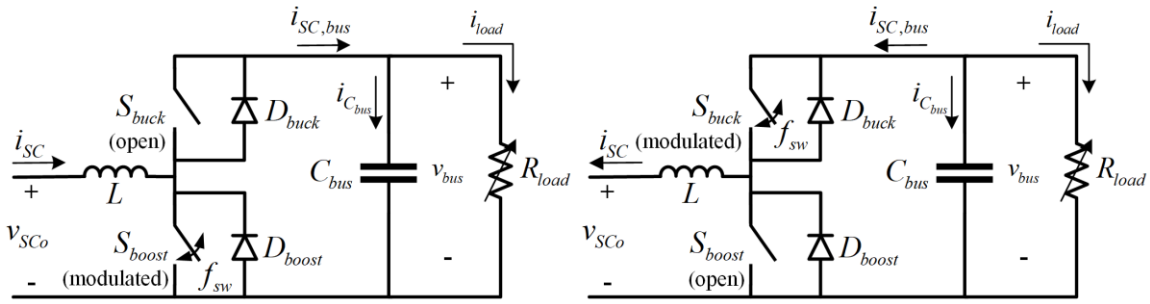

Figure 11. SC BBC Operation (Left: Boost Mode; Right: Buck Mode)

The bus voltage depends on the duty cycle of the switch being modulated in either mode. Because $v_{Bo}(t)$ and $v_{SCo}(t)$ vary over time and there are two BBCs connected in parallel, there is no closed form equation that relates the bus voltage $v_{bus}(t)$ to the battery or SC duty cycles. Instead, assuming that the converter inductance L, bus capacitance

C_{bus}, and switching frequency f_{sw} are sufficiently high to keep the BBCs in continuous conduction mode (CCM), and neglecting converter losses, we can calculate the bus currents $i_{B,bus}(t)$ and $i_{SC,bus}(t)$ using the following conservation of power relationships:

$$v_{Bo}(t)i_B(t) = v_{bus}(t)i_{B,bus}(t) \tag{26}$$

and

$$v_{SCo}(t)i_{SC}(t) = v_{bus}(t)i_{SC,bus}(t)\,. \tag{27}$$

Applying Kirchhoff's Current Law (KCL) at node "A" in Figure 9 gives the total bus current created by the HESS $i_{HESS,bus}(t)$ as

$$i_{HESS,bus}(t) = i_{B,bus}(t) + i_{SC,bus}(t)\,. \tag{28}$$

2. Photovoltaic Panels

As shown in Figure 9, PV panels are connected in parallel with the HESS through a unidirectional boost converter. For the purposes of this simulation, the PV panels are assumed to be ideal power sources that supply the power profile $P_{PV}(t)$ shown in Figure 12 (representative of an idealized daily PV panel power profile [30]) directly to the bus. Over a typical 24-hour period, the PV panels deliver a total of 29 kWh to the DC bus. The converter inductance L, bus capacitance C_{bus}, and switching frequency f_{sw} are once again assumed to be sufficiently large to maintain CCM and the switching losses are neglected. Similar to the conservation of power relationships in (26) and (27), the bus current contributed by the PV panels $i_{PV,bus}(t)$ is

$$i_{PV,bus}(t) = \frac{P_{PV}(t)}{v_{bus}(t)}\ . \tag{29}$$

Applying KCL at node "B" in Figure 9 gives the total bus current $i_{bus}(t)$ as

$$i_{bus}(t) = i_{HESS,bus}(t) + i_{PV,bus}(t)\ . \tag{30}$$

To prevent sudden transients in the PV supply power, the PV power profile $P_{PV}(t)$ is filtered using the following transfer function:

$$T_{LPF,PV}(s) = \frac{1}{\tau_{PV}s + 1}. \tag{31}$$

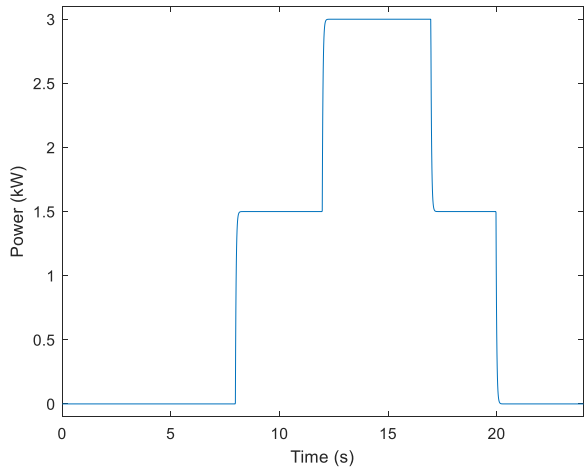

Figure 12. Photovoltaic Panel Power Profile

3. Resistive Load and Bus Capacitance

The load placed on the DC bus in this simulation is purely resistive. Over the 24-hour period, the load resistance $R_{load}(t)$ changes to create the power profile shown in Figure 13 (representative of the typical daily power consumption in a remote military microgrid [14]). This nominal resistive load demands a total energy of 118 kWh daily.

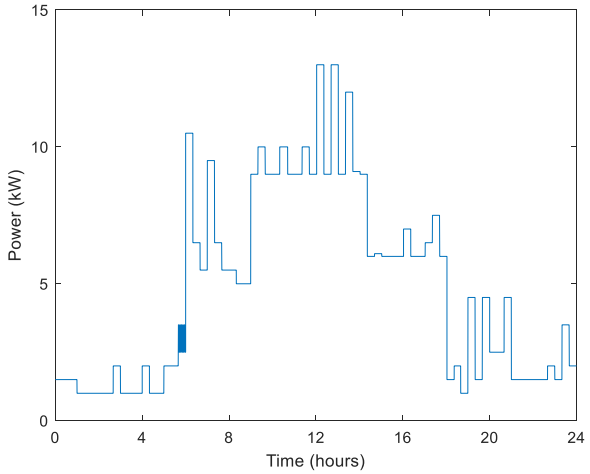

Figure 13. Daily Load Profile in a Military Microgrid. Adapted from [14].

Applying KCL at Node B in Figure 9, we obtain the bus capacitance current

$$i_{C_{bus}}(t) = i_{bus}(t) - i_{load}(t) = i_{bus}(t) - \frac{v_{bus}(t)}{R_{load}(t)} \ , \tag{32}$$

where the bus voltage $v_{bus}(t)$ can be found using

$$v_{bus}(t) = v_{bus}(0) + \frac{1}{C_{bus}} \int_0^t i_{C_{bus}}(\tau) d\tau \ . \tag{33}$$

4. DC Bus Voltage Controller

The DC bus voltage is controlled using a PI controller that drives the error between the bus voltage and a constant reference voltage to zero by adjusting the total current demanded from the HESS elements $i_{HESS}(t)$. If the SC bank is connected, then $i_{HESS}(t)$ is passed through a unity passband gain LPF with transfer function

$$T_{LPF}(s) = \frac{1}{\tau_{LPF} s + 1} \tag{34}$$

and time constant τ_{LPF} to the battery bank and through a HPF with transfer function

$$T_{HPF}(s) = K_{HPF} \frac{\tau_{HPF} s}{\tau_{HPF} s + 1} \ , \tag{35}$$

adjustable passband gain K_{HPF}, and time constant τ_{HPF} to the SC bank. If the SC bank is disconnected, then $i_B(t) = i_{HESS}(t)$ and $i_{SC}(t) = 0$. The battery and SC currents are limited to the intervals $-N_{Bp} i_{Bmax} < i_B(t) < N_{Bp} i_{Bmax}$ and $-N_{SCp} i_{SCmax} < i_{SC}(t) < N_{SCp} i_{SCmax}$, respectively.

B. SIMULINK MODEL

The top-level SIMULINK model of the islanded DC microgrid is shown in Figure 14. The components are color-coded to illustrate the implementation of (26)-(28) and (30)-(32). This model produces four matrices of outputs: **data_batt**, **data_sc**, **data_pv**, and **data_load**. These output matrices provide all of the necessary data for the analysis performed in this chapter, and their components are individually labeled in Figure 14.

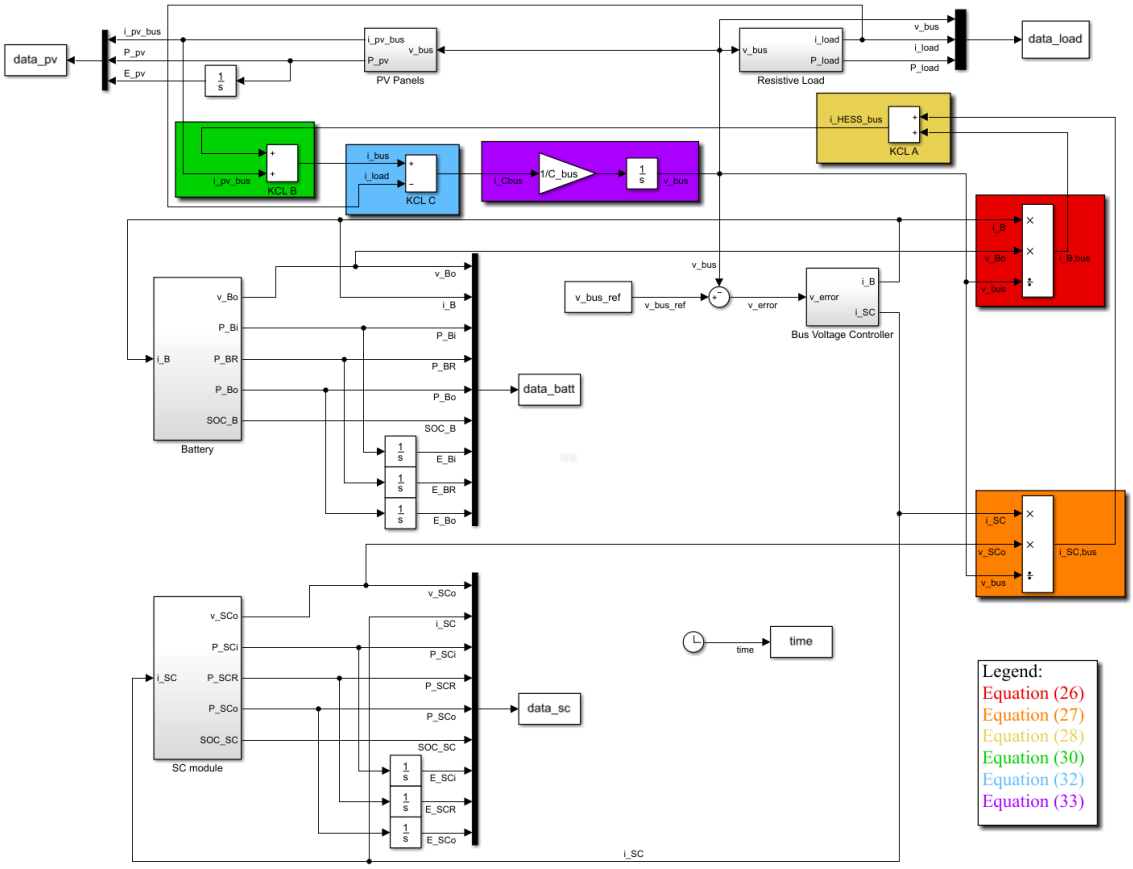

Figure 14. Islanded DC Microgrid SIMULINK Model

The subsystem model of the resistive load is shown in Figure 15. The lookup table is loaded with a vector of inverse resistances required to create the power profile shown in Figure 13 (with 2-minute resolution).

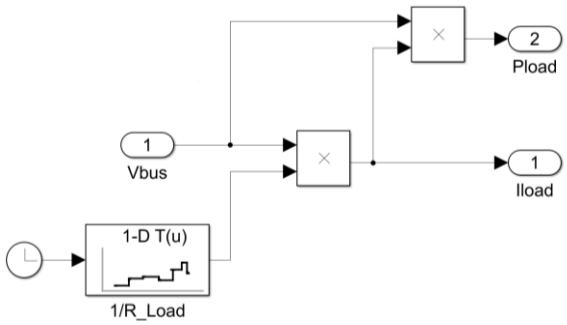

Figure 15. Resistive Load SIMULINK Model

The subsystem model of the bus voltage controller is shown in Figure 16. The filter transfer functions, SC connection status, and saturation values are implemented as previously stated. Adjusting the HPF passband gain K_{HPF} changes the amount of current demand that is diverted to the SC bank during a load transient.

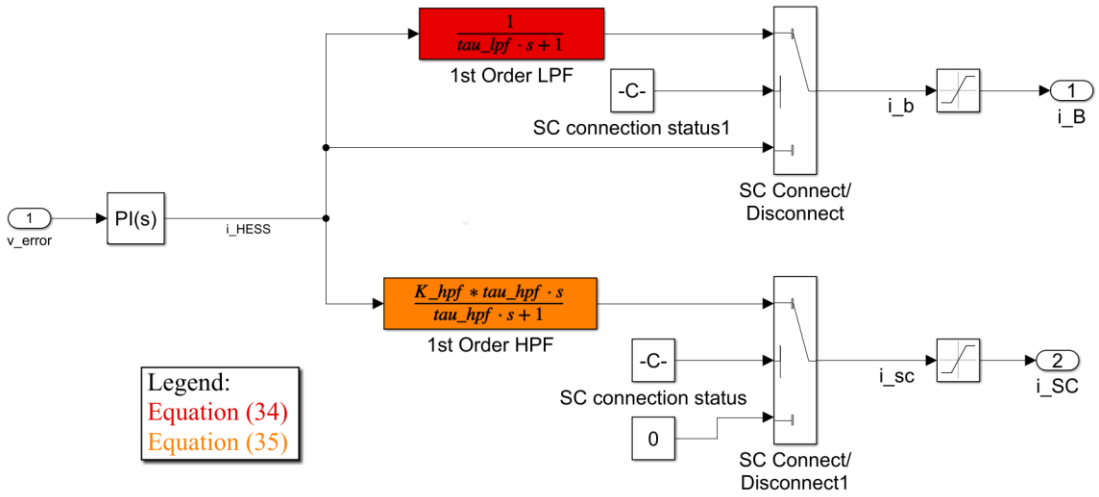

Figure 16. Bus Voltage Controller SIMULINK Model

The subsystem model of the PV panel array is shown in Figure 17. The lookup table is loaded with a vector of power values that create the profile shown in Figure 12 (with 2-minute resolution). The PV power profile is filtered using (31), and the output bus current is calculated using (29), as shown.

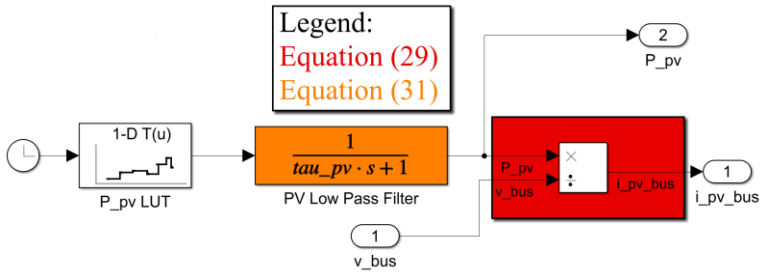

Figure 17. PV Panel SIMULINK Model

C. PARAMETERS

The islanded DC microgrid simulation parameters are listed in Table 3. The lead-acid battery bank is designed so that, for the 24-hour power profile being simulated, the overall state-of-charge $SOC_B(t)$ stays positive and the battery bank terminal voltage $v_{Bo}(t)$ stays below the reference bus voltage $V_{bus,ref}$ (200 V). Since the load demands 118 kWh and the PV panels produce 29 kWh during this 24-hour simulation, the HESS is responsible for producing 89 kWh. The battery bank is conservatively designed for a nominal capacity of 100 kWh. Each lead-acid battery holds 144 W·h when fully charged; therefore, the lead-acid battery bank requires a total of 695 lead-acid batteries. To achieve a nominal battery terminal voltage $v_{Bo}(t)$ of 180 V (10% less than $V_{bus,ref}$) and meet this sizing requirement, values of 15 and 47 were chosen for N_{Bs} and N_{Bp}, respectively.

The SC bank is designed to be able to produce up to 5% of the energy that the HESS is required to provide to the load (4.45 kWh). Each SC holds 57 W·h when fully charged; therefore, the SC bank requires a total of 78 SCs. To achieve an initial SC bank voltage of 168 V (16% less than $V_{bus,ref}$), values of 3 and 26 were chosen for N_{SCs} and N_{SCp}, respectively.

The input current filter time constants τ_{LPF} and τ_{HPF} as well as the PV filter time constant τ_{PV} were all set to 120 s to match the time resolution on the $P_{load}(t)$ and $P_{PV}(t)$ data vectors. The cutoff frequency corresponding to this time constant is $f_c = 1/2\pi\tau = 1.326 \cdot 10^{-3}$ Hz. The HPF passband gain K_{HPF} was set to 25 to make the SCs sufficiently responsive to large transients in $P_{load}(t)$. Because the model contains so many nonlinearities, there is no closed-form equation that can be used to determine suitable bus voltage PI controller gains $K_{p,v}$ and $K_{i,v}$. For this particular load profile, the gains were set to 0.5 and 0.1, respectively, and the simulation time step t_{step} was set to 0.1 s. For simulations with larger power transients, the PI gains as well as t_{step} may need to be reduced to avoid simulation errors.

Table 3. Islanded DC Microgrid Simulation Parameters

Parameter	Symbol	Value	Units
Lead-acid batteries in series	N_{Bs}	15	
Lead-acid battery branches in parallel	N_{Bp}	47	
Supercapacitors in series	N_{SCs}	3	
Supercapacitor branches in parallel	N_{SCp}	26	
Bus capacitance	C_{bus}	0.5	F
Reference bus voltage	$V_{bus,ref}$	200	V
Filter time constants	$\tau_{LPF} = \tau_{HPF} = \tau_{PV}$	120	s
Filter cutoff frequency	f_c	1.326	mHz
HPF passband gain	K_{HPF}	25	
Voltage controller proportional gain	$K_{p,v}$	0.5	
Voltage controller integral gain	$K_{i,v}$	0.1	
Simulation time step	t_{step}	0.1	s

D. RESULTS

The results of the islanded DC microgrid simulation illustrate some of the advantages to implementing a battery and supercapacitor HESS over a traditional battery energy storage system. Implementing the microgrid model shown in Figure 14 and the bus voltage control scheme shown in Figure 16 reduces the average power delivered to internal resistances within the HESS, successfully removes the high-frequency component of the battery current, reduces the daily depletion of the battery bank SOC, and significantly reduces the energy lost to internal resistances over the 24-hour simulation period.

1. Power Totals

As shown in Figure 18, when the SC bank is disconnected, the lead-acid battery bank and PV panels supply sufficient steady-state power to the load. Because the batteries supply a majority of the energy to the load in this simulation, the resistive loss power plot closely resembles the shape of the load profile in Figure 13.

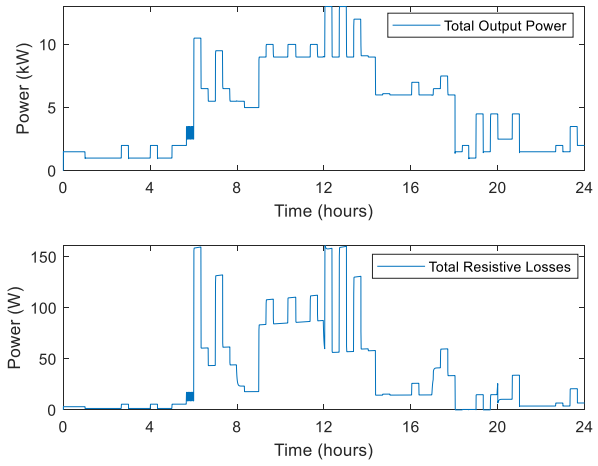

Figure 18. Islanded DC Microgrid: Power Totals (SCs Disconnected)

The improvements made to the power flow within this DC microgrid model by connecting the SC bank can be seen in Figure 19. When the SCs are connected, the power lost to internal resistances within the HESS components is significantly lower on average due to the SC equivalent series resistance R_{esr} being approximately 20 times smaller than the battery resistance R_B.

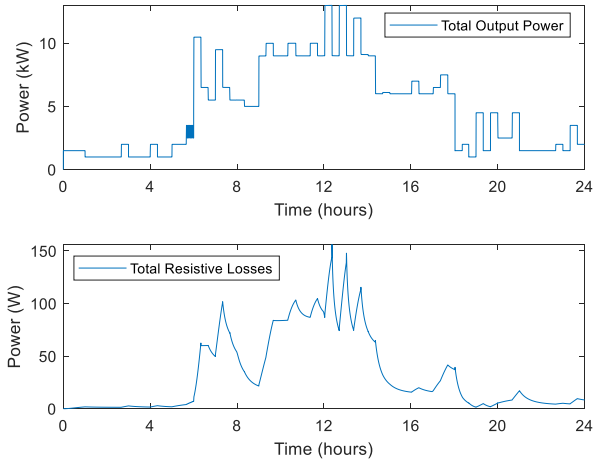

Figure 19. Islanded DC Microgrid: Power Totals (SCs Connected)

2. HESS Currents

One goal of implementing the HESS control scheme shown in Figure 16 is to divert the high-frequency components of the total HESS current demand i_{HESS} to the SC bank. This reduces the cyclical stress on the lead-acid battery bank, which has been shown to improve battery lifetime [10], [14]. As shown in Figure 20, when the SC bank is disconnected, $i_B(t)$ responds in approximately 30 s to step changes in load demand. When the SC bank is connected, $i_B(t)$ takes nearly three hours to settle after step changes in load demand; therefore, the proposed modeling scheme effectively diverts the high-frequency HESS current demand components to the SC bank.

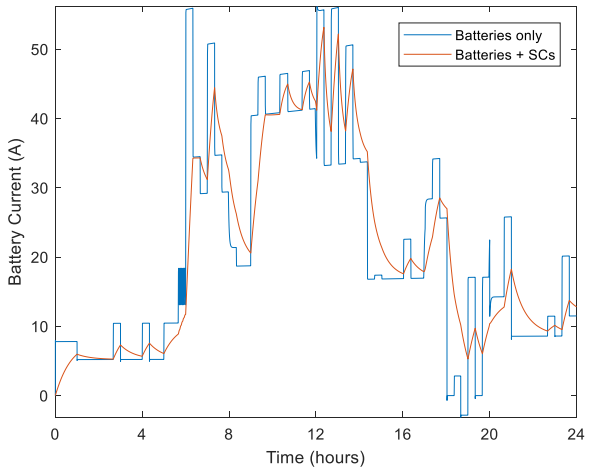

Figure 20. Islanded DC Microgrid: Battery Current (SCs Disconnected versus Connected)

The HESS currents $i_B(t)$ and $i_{SC}(t)$ are both plotted in Figure 21 to show how $i_{HESS}(t)$ is divided between the battery bank and SC bank when the SCs are connected in islanded mode. As expected, $i_B(t)$ remains positive for the 24-hour simulation period, but $i_{SC}(t)$ is positive following step increases in load demand and negative following step decreases in load demand.

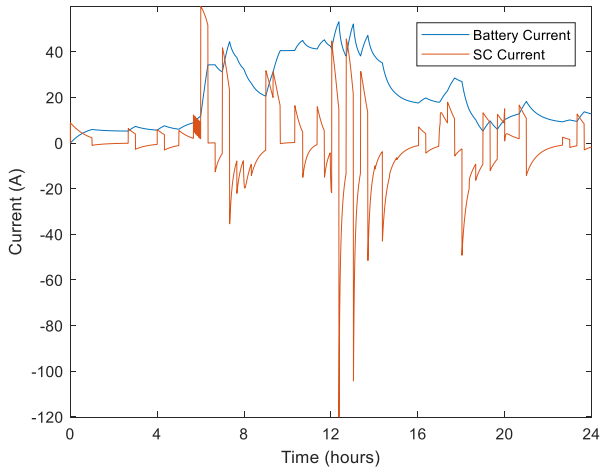

Figure 21. Islanded DC Microgrid: HESS Currents (SCs Connected)

3. State of Charge

The proposed HESS control scheme is expected to reduce the daily battery SOC drain when compared with a traditional lead-acid battery energy storage system. As shown in Figure 22, connecting the SC bank to the islanded DC microgrid makes $SOC_B(t)$ much smoother and increases the final value of $SOC_B(t)$ by 1.214%. As shown in Figure 20, connecting the SC bank increases the transient values of $i_B(t)$ at step decreases in load demand; therefore, the daily battery SOC drain can be further improved by decreasing τ_{LPF} and τ_{HPF} during decreases in load demand and increasing τ_{LPF} and τ_{HPF} during increases in load demand. This requires a more sophisticated control and filtering scheme and would make the simulation significantly more computationally intensive.

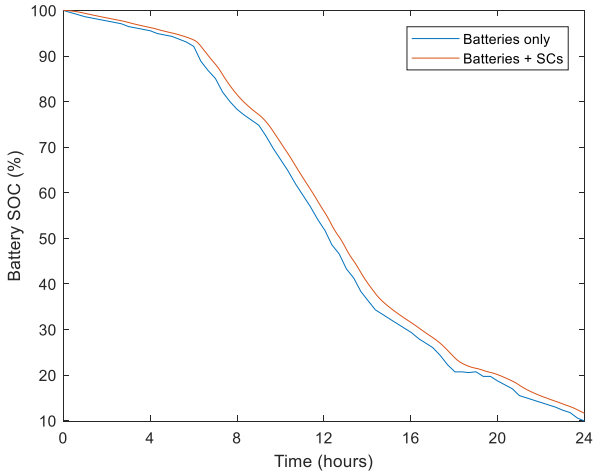

Figure 22. Islanded DC Microgrid: Battery SOC (SCs Disconnected versus Connected)

As illustrated in Figure 23, $SOC_B(t)$ and $SOC_{SC}(t)$ remain within acceptable ranges, which indicates that the HESS is properly sized for islanded microgrid operation. For the proposed islanded HESS dimensions, $SOC_B(t)$ remains positive (as designed) and $SOC_{SC}(t)$ remains above 2.5% for the SC bank dimensions chosen for this simulation.

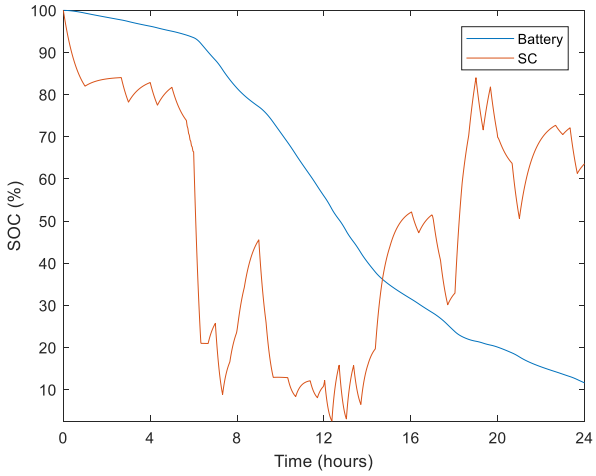

Figure 23. Islanded DC Microgrid: Battery and SC SOC (SCs Connected)

4. Energy Savings

Because this simulation only models the internal resistances of the lead-acid battery and SC banks and assumes all other components are ideal and lossless, the overall power efficiency is not a useful calculation. The energy lost to the internal resistances, however, provides a useful and meaningful metric for quantifying the improvements made to the energy efficiency of the microgrid using the proposed control scheme. In this simulation, connecting the SC bank reduces the energy lost to internal resistances from 851 W·h to 779.8 W·h, giving an 8.37% reduction in lost energy. These losses scale with the size of the load demand and the HESS banks; therefore, for larger systems, these energy savings could have a significant impact on the overall microgrid operation cost.

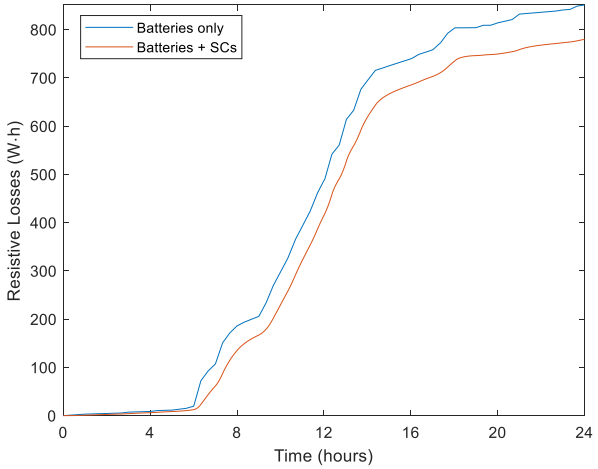

Figure 24. Islanded DC Microgrid: Resistive Losses (SCs Disconnected versus Connected)

When the SCs are connected, the energy savings depend heavily on the HPF passband gain. Increasing K_{HPF} is expected to make the SCs more responsive to high-frequency HESS current ripples and, therefore, reduce the daily energy loss due to internal resistances within the HESS. As shown in Figure 25, for low K_{HPF}, the energy savings are minimal, and the largest energy savings can be achieved at $K_{HPF} \approx 25$. Values greater than 28 make the islanded DC microgrid simulation unstable.

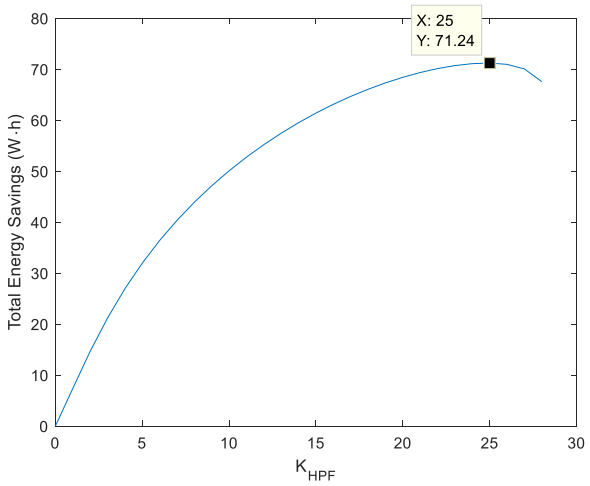

Figure 25. Islanded DC Microgrid: Effect of K_{HPF} on Overall Energy Savings

THIS PAGE INTENTIONALLY LEFT BLANK

V. GRID-CONNECTED DC MICROGRID SIMULATION

A grid-connected DC microgrid model is created to simulate a 24-hour load profile sourced by HESS elements, PV panels, and a 5-kW generator. The additional system components, modified SIMULINK model, HESS sizing procedure, and simulation results are explained in this chapter.

A. ADDITIONAL SYSTEM COMPONENTS

A block diagram of the grid-connected microgrid model is shown in Figure 26. In the context of this thesis, a "grid-connected" microgrid is connected to non-renewable power sources, such as generators (as would be found at a standard military FOB). The theory and implementation of the simulated local utility grid are explained in this section.

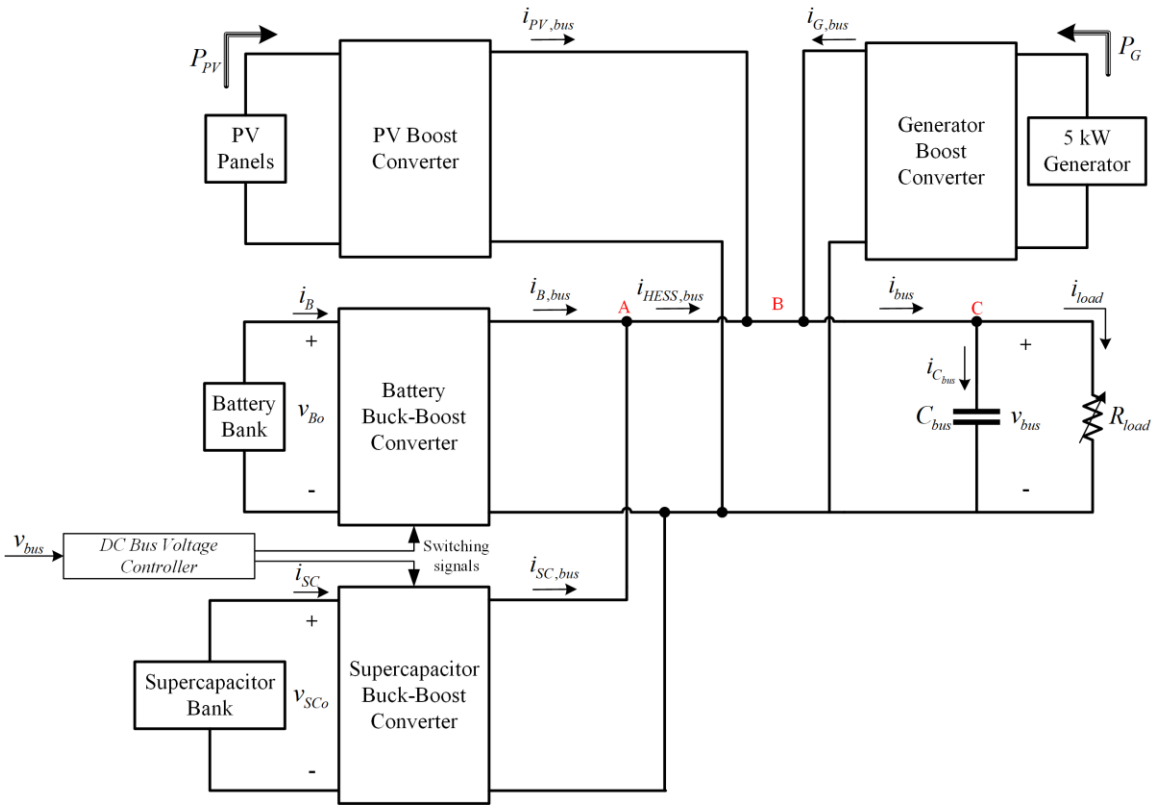

Figure 26. Grid-Connected DC Microgrid Block Diagram

1. Local Grid

In this simulation, the local grid is implemented as an ideal 5-kW generator that produces the power profile shown in Figure 27 (similar to the grid implementation in [14]). The generator is only turned on during peak-power consumption periods (0600–0800 and 0900–1400) and delivers 35 kWh to the DC bus daily. Similarly to the PV panels, the generator is connected to the DC bus through a unidirectional boost converter. Applying conservation of power across the generator boost converter gives the generator bus current $i_{G,bus}(t)$ as

$$i_{G,bus}(t) = \frac{P_G(t)}{v_{bus}(t)} \ . \tag{36}$$

Applying KCL at node "B" in Figure 26 gives the total bus current $i_{bus}(t)$ as

$$i_{bus}(t) = i_{HESS,bus}(t) + i_{PV,bus}(t) + i_{G,bus}(t) \ . \tag{37}$$

To prevent sudden transients in the generator supply power, the generator power profile $P_G(t)$ is filtered using the transfer function

$$T_{LPF,G}(s) = \frac{1}{\tau_G s + 1} . \tag{38}$$

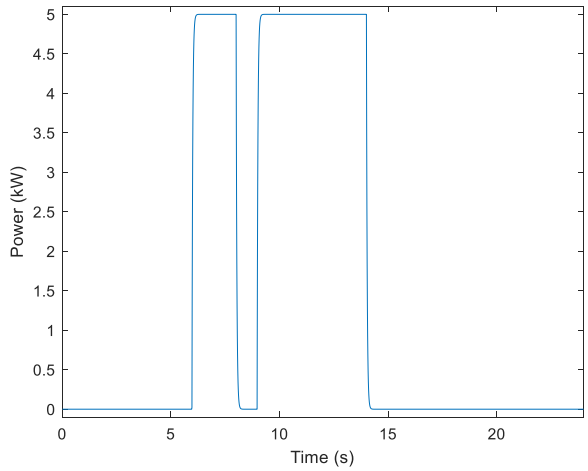

Figure 27. 5-kW Generator Power Profile

B. MODIFIED SIMULINK MODEL

The top-level SIMULINK model of the grid-connected DC microgrid is shown in Figure 28. The implementation of the generator is outlined with a gray box, and the generator subsystem model is shown in Figure 29. The lookup table is loaded with a vector of power values that create the profile shown in Figure 27 (with 2-minute resolution). The generator power profile is filtered using (38), and the output bus current is calculated using (36), as shown. All other components are modeled and implemented as described in Figures 12–17 and (26)-(29) and (31)-(35).

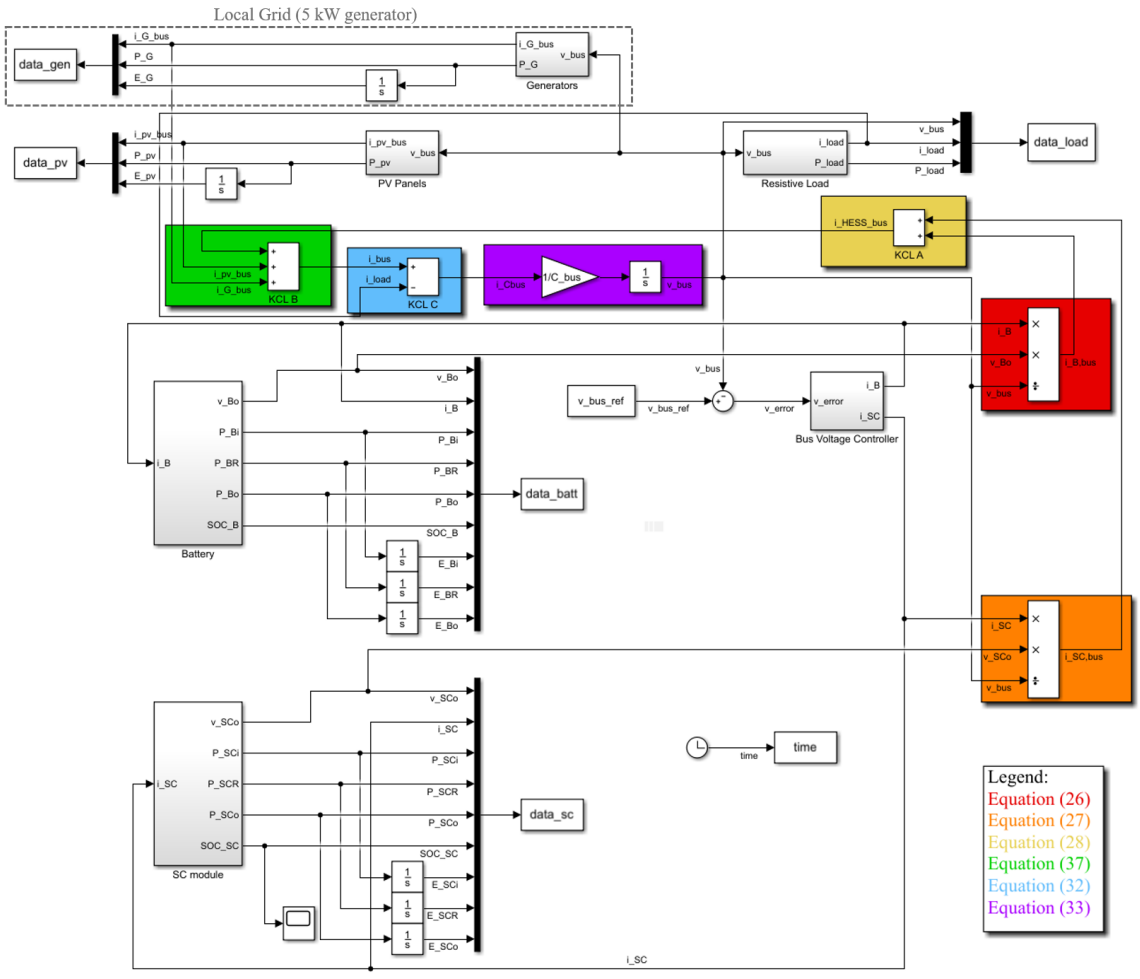

Figure 28. Grid-Connected DC Microgrid SIMULINK Model

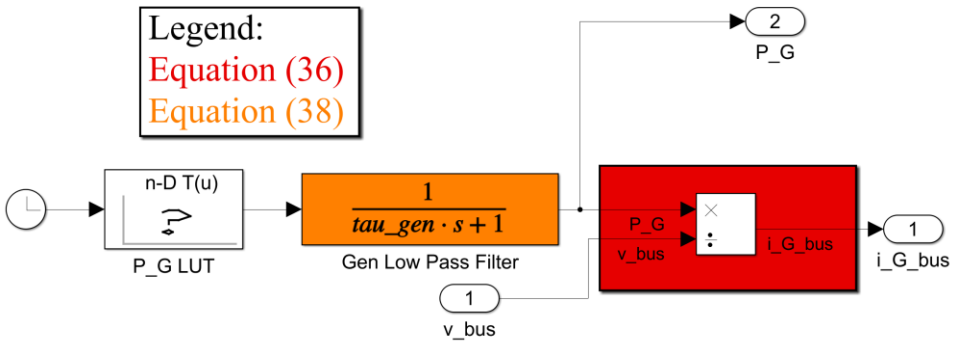

Figure 29. 5-kW Generator SIMULINK Model

C. PARAMETERS

The grid-connected DC microgrid simulation parameters are listed in Table 4 with the values from Table 3 included in parentheses for comparison. The lead-acid battery and SC banks are designed using the same procedure that was used to size the HESS for the islanded DC microgrid. Since the load demands 118 kWh, the PV panels produce 29 kWh, and the generators produce 35 kWh during this 24-hour simulation, the HESS is responsible for supplying 54 kWh. The battery bank is conservatively designed for a nominal capacity of 60 kWh. Each lead-acid battery holds 144 W·h when fully charged; therefore, the lead-acid battery bank requires a total of 416 lead-acid batteries. To achieve a nominal battery terminal voltage $v_{Bo}(t)$ of 180 V (10% less than $V_{bus,ref}$) and meet this sizing requirement, values of 15 and 28 were chosen for N_{Bs} and N_{Bp}, respectively. This lead-acid battery bank is 40.9% smaller than the one required for the islanded DC microgrid.

The SC bank is designed to be able to store up to 5% of the energy that the HESS is required to provide to the load (2.7 kWh). Each SC holds 57 W·h when fully charged; therefore, the SC bank requires a total of 48 SCs. To achieve an initial SC bank voltage of 168 V (16% less than $V_{bus,ref}$), values of 3 and 16 were chosen for N_{SCs} and N_{SCp}, respectively. This SC bank is 38.5% smaller than the one required for the islanded DC microgrid.

As listed in Table 4, all other parameters for the grid-connected DC microgrid simulation have the same value as their counterparts in the islanded DC microgrid simulation to ensure a fair comparison between HESS sizes.

Table 4. Grid-Connected DC Microgrid Simulation Parameters

Parameter	Symbol	Value	Units
Lead-acid batteries in series	N_{Bs}	15 (15)	
Lead-acid battery branches in parallel	N_{Bp}	28 (47)	
Supercapacitors in series	N_{SCs}	3 (3)	
Supercapacitor branches in parallel	N_{SCp}	16 (26)	
Bus capacitance	C_{bus}	0.5 (0.5)	F
Reference bus voltage	$V_{bus,ref}$	200 (200)	V
Filter time constants	$\tau_{LPF} = \tau_{HPF} = \tau_{PV}$	120 (120)	s
Filter cutoff frequency	f_c	1.326 (1.326)	mHz
HPF passband gain	K_{HPF}	25 (25)	
Voltage controller proportional gain	$K_{p,v}$	0.5 (0.5)	
Voltage controller integral gain	$K_{i,v}$	0.1 (0.1)	
Simulation time step	t_{step}	0.1 (0.1)	s

D. RESULTS

When compared to the islanded DC microgrid results, the results of the grid-connected DC microgrid simulation reinforce the previously explained advantages to implementing a battery and supercapacitor HESS. These results also quantify the effects of grid connection on HESS sizing requirements for this particular combination of load and source power profiles.

1. Power Totals

As shown in Figures 30 and 31, the total output power for both cases (SCs disconnected and SCs connected) matches the load profile shown in Figure 13. Compared to the values plotted in Figures 18 and 19, these resistive loss power plots have similar

trends, but the loss power values are nearly halved when the lossless 5-kW generator is connected to the microgrid.

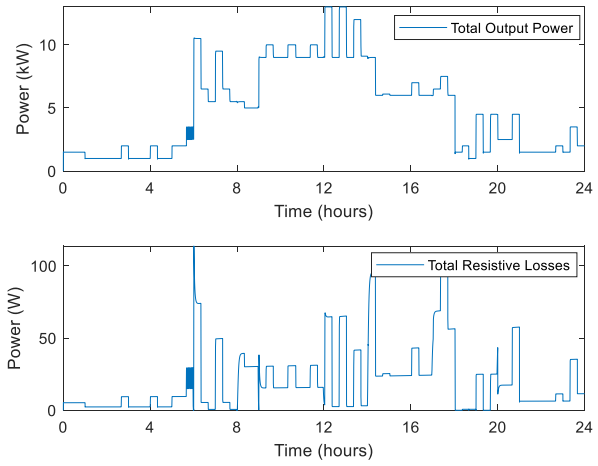

Figure 30. Grid-Connected DC Microgrid: Power Totals (SCs Disconnected)

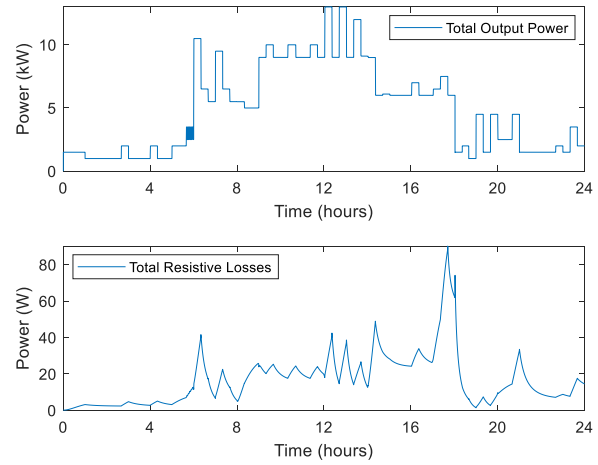

Figure 31. Grid-Connected DC Microgrid: Power Totals (SCs Connected)

2. HESS Currents

The grid-connected HESS current plots also have similar shapes but different magnitudes when compared to the islanded HESS current plots. As shown in Figure 32,

similar to the plots in Figure 20, when the SCs are connected, $i_B(t)$ tracks the low frequency component of $i_{HESS}(t)$. When the generator is active, $i_B(t)$ is reduced by 50% to 58% in both cases (SCs disconnected and SCs connected).

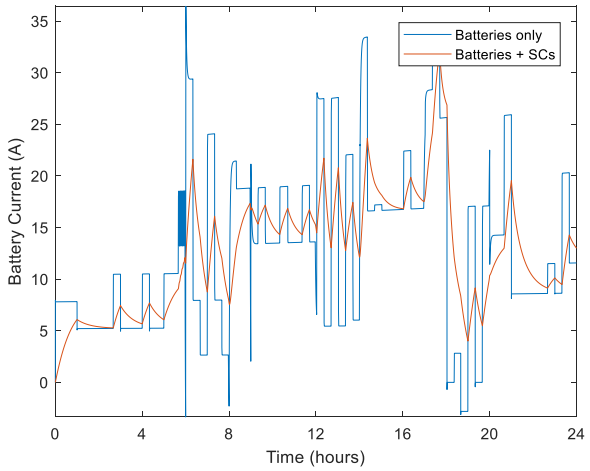

Figure 32. Grid-Connected DC Microgrid: Battery Current (SCs Disconnected versus Connected)

The HESS currents $i_B(t)$ and $i_{SC}(t)$ are both plotted in Figure 33 to show how $i_{HESS}(t)$ is divided between the battery bank and SC bank when the SCs are connected in grid-connected mode. As expected, connecting the generators significantly reduces $i_{SC}(t)$ and, during periods of peak PV and generator power production as well as during large decreases in $P_{load}(t)$, $i_{SC}(t)$ reaches negative transient values of up to −90.4 A.

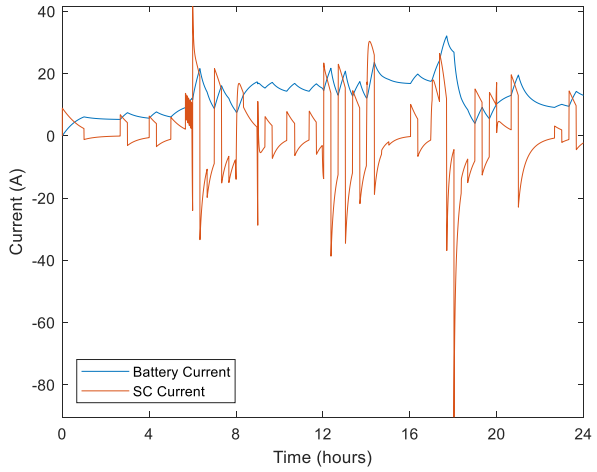

Figure 33. Grid-Connected DC Microgrid: HESS Currents (SCs Connected)

3. State of Charge

In grid-connected mode, implementing the HESS controller as proposed successfully reduces the daily battery SOC depletion. As shown in Figure 34, connecting the SC bank to the grid-connected microgrid increases the final value of $SOC_B(t)$ by 1.214% and, similar to the trends observed in Figure 22, makes the plot of $SOC_B(t)$ much smoother.

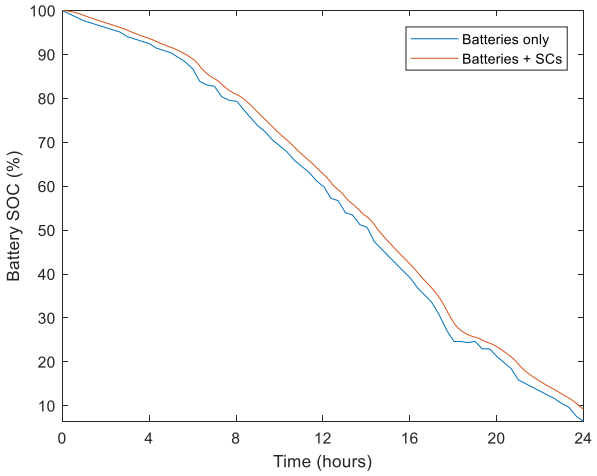

Figure 34. Grid-Connected DC Microgrid: Battery SOC (SCs Disconnected vs Connected)

As illustrated in Figure 35, $SOC_B(t)$ and $SOC_{SC}(t)$ (similarly to Figure 23), the SOCs of both HESS elements remain within acceptable ranges, which indicates that the HESS is properly sized for grid-connected operation. For the proposed grid-connected HESS dimensions, $SOC_B(t)$ remains positive (as designed) and $SOC_{SC}(t)$ remains above 3% for the SC bank dimensions chosen for this simulation.

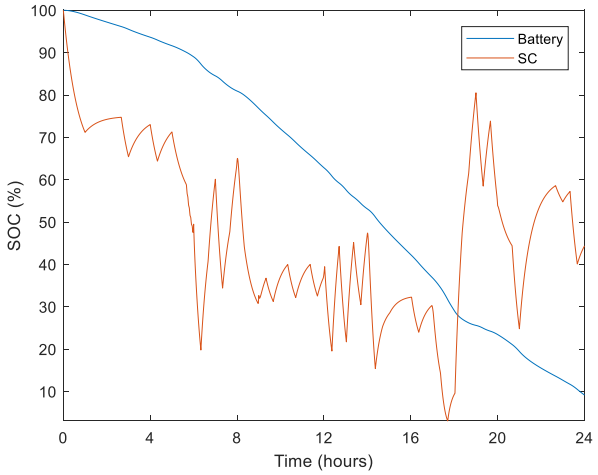

Figure 35. Grid-Connected DC Microgrid: Battery and SC SOC (SCs Connected)

4. Energy Savings

The cumulative energy lost to internal resistances within the grid-connected HESS (R_B and R_{esr}) is plotted with respect to time for both cases (SCs disconnected and SCs connected) in Figure 36. By comparing the final values of each plot, it can be seen that connecting the SC bank reduces the energy lost to internal resistances from 490.4 W·h to 403.4 W·h, giving a 17.7% reduction in lost energy. Because the losses within the generator, connections, and lines are not calculated, this proportional energy saving value is over double the value observed for the islanded DC microgrid simulation (8.37%). This result indicates that integrating additional power sources into the microgrid model allows for smaller battery and SC bank sizing, which increases the proportional energy savings

that can be attained by implementing the HESS when compared to a traditional battery energy storage system.

The effects of K_{HPF} on overall savings within the grid-connected HESS are very similar to the observations made in the islanded DC microgrid simulation results. As shown in Figure 37, similar to Figure 25, the energy savings are minimal for low K_{HPF}, and the largest energy savings are achieved at $K_{HPF} \approx 26$. The maximum possible energy savings for the grid-connected DC microgrid (86.98 W·h) is 22.1% higher than the maximum energy savings for the islanded DC microgrid (71.24 W·h). Values greater than 28 make the grid-connected DC microgrid simulation unstable.

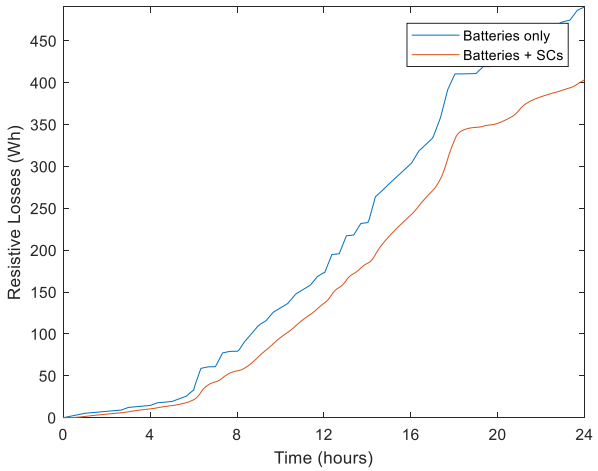

Figure 36. Grid-Connected DC Microgrid: Resistive Losses (SCs Disconnected versus Connected)

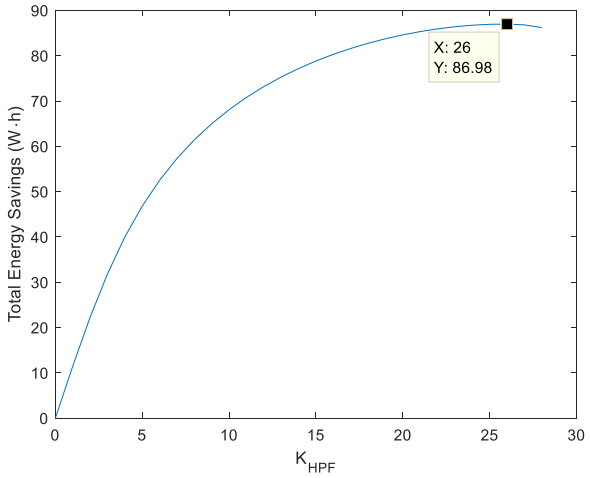

Figure 37. Grid-Connected DC Microgrid: Effect of K_{HPF} on Overall Energy Savings

THIS PAGE INTENTIONALLY LEFT BLANK

VI. CONCLUSIONS AND FUTURE WORK

The models, simulations, and results described in this thesis lead to the conclusions described in this section. There are several opportunities for follow-on work that can advance this line of research to implementation at military FOBs.

A. CONCLUSIONS

The primary research objective of this thesis was to model the exchange of electrical energy and power between the source, storage, and load elements in a simulated EMS-controlled microgrid with a battery and SC HESS. Fulfilling this objective for the combination of load and source power profiles simulated in this thesis led to several notable observations. Based on the results for both the islanded and grid-connected DC microgrid simulations, implementing the proposed HESS controller successfully removes the high-frequency component of the battery current, reduces the daily depletion of the battery bank SOC, and significantly reduces the energy lost to internal resistances over the 24-hour simulation period. These benefits are more significant in grid-connected mode than in islanded mode because connecting additional power sources to the microgrid allows for smaller and more energy-efficient HESS sizing. This difference can be seen most clearly by comparing the proportional energy savings in both scenarios; for these test cases, in grid-connected mode, implementing the HESS reduces energy losses by over twice the percentage that it is reduced in islanded mode.

Secondary objectives of this thesis included improving the sizing of the SC and battery elements of the HESS and quantifying the overall efficiency of the modeled microgrid system. Whereas previous models and simulations did not account for the effects of state-of-charge or internal resistances on HESS terminal voltages and current demands [26], the models described in this thesis provide a first-order approximation of these effects and serve as a useful tool for investigating the effects of HESS sizing on EMS performance. These models are scalable and can easily be modified to simulate any set of input and load power profiles. For the test cases simulated in this thesis, sizing the battery and SC banks to store 110% and 5% of the HESS energy requirement, respectively, maintains $SOC_B(t)$

and $SOC_{SC}(t)$ within acceptable limits. By comparing the daily energy losses to internal HESS resistances, we can use the simulation results obtained in this thesis to quantify the efficiency improvement gained by implementing a battery and SC HESS compared to using a traditional lead-acid battery storage system.

B. RECOMMENDATIONS FOR FUTURE WORK

There are several opportunities to continue the work accomplished in this thesis with follow-on modeling and simulations. First of all, the losses within the connections, lines, and protection circuits within both the lead-acid batteries and SC modules are not accounted for in these models. The internal resistance values used in the SIMULINK models are based on manufacturer specifications but need to be verified through laboratory experimentation. Additionally, the losses within the buck-boost converters, PV panels, and generator should be modeled in future research efforts to increase the precision of the simulation results.

These models should also be tested for different sets of source and load power profiles based on available data from military microgrids. The profiles simulated in this thesis are based on scaled-down nominal load and source power data [14], but the scalability of these models allows the power magnitudes to be easily adjusted. When increasing the scale of the system, it may be necessary to decrease the simulation time step t_{step} and adjust the PI controller gains $K_{p,v}$ and $K_{i,v}$ as well as the HPF gain K_{HPF} to achieve similar results.

Future studies in this line of research should investigate the performance of these HESS models in single-phase AC microgrid simulations. The results obtained in this thesis show that the DC bus voltage controller is capable of maintaining $v_{bus}(t)$ within acceptable margins of its nominal value (200 V). The DC bus needs to be connected to a controllable PWM inverter, which can then be connected to a local AC grid and AC loads as done in [5], [14], [26], and [30]. Integrating an inverter into this model would likely introduce new harmonics into the HESS current demands, which would require a more sophisticated control scheme than the one proposed in this thesis.

APPENDIX: MATLAB SCRIPTS

```
% islanded_parameters_24hr.m
% Sets parameters for islanded DC microgrid simulation
% time parameters:
tstep = 0.1;
tstop = 86400; % 10 hours for now, will be 24 hours later
% battery parameters:
N_Bs = 15;
N_Bp = 47;
R_B = 16e-3*10; % ohms
SOC_Bmax = 12; % A hr
SOC_B0 = SOC_Bmax; % A hr
SOC_B_data_vector = (0:100); % percent
v_Bimax = 12.86; % V (for each series element)
v_Bi_data_vector = 11.5:0.0136:v_Bimax; % V
i_Bmax = 40; % A (for each parallel branch)
% sc parameters:
N_SCs = 3;
N_SCp = 26;
R_esr = 8.1e-3; % ohms
SOC_SCmax = 57; % W hr
SOC_SC0 = SOC_SCmax; % W hr
C_sc = 130; % F
v_SCimax = sqrt(2*SOC_SCmax*3600/C_sc); % V (for each
series element)
i_SCmax = 1900; % A (for each parallel branch)
% filter parameters:
tau_lpf = 120;
fc_lpf = 1/(2*pi*tau_lpf);
tau_hpf = 120;
fc_hpf = 1/(2*pi*tau_hpf);
Kp_v = 0.5;
Ki_v = 0.1;
K_hpf = 25;
% bus voltage parameters
C_bus = 0.5;
v_bus_ref = 200;
% load parameters
load('Load')
R_load_inv = P_load/v_bus_ref^2;
% PV panel parameters
load('PV')
tau_pv = 120;
```

```
% islanded_script_24hr.m
% Simulates islanded DC microgrid model over 24 hours
% for SCs disconnected and SCs connected
% Generates Figures 12-13, 18-25
clear all
close all
clc
% generates data for simulation with BATTERIES ONLY
sc_connection_status = 0;
sim('islanded_model_24hr')
v_batt_0 = data_batt(:,1);
i_batt_0 = data_batt(:,2);
p_batt_in_0 = data_batt(:,3);
p_batt_lost_0 = data_batt(:,4);
p_batt_out_0 = data_batt(:,5);
SOC_batt_0 = data_batt(:,6);
E_batt_in_0 = data_batt(:,7);
E_batt_lost_0 = data_batt(:,8);
E_batt_out_0 = data_batt(:,9);
v_sc_0 = data_sc(:,1);
i_sc_0 = data_sc(:,2);
p_sc_in_0 = data_sc(:,3);
p_sc_lost_0 = data_sc(:,4);
p_sc_out_0 = data_sc(:,5);
SOC_sc_0 = data_sc(:,6);
E_sc_in_0 = data_sc(:,7);
E_sc_lost_0 = data_sc(:,8);
E_sc_out_0 = data_sc(:,9);
v_load_0 = data_load(:,1);
i_load_0 = data_load(:,2);
p_load_0 = data_load(:,3);
i_pv_0 = data_pv(:,1);
p_pv_0 = data_pv(:,2);
E_pv_0 = data_pv(:,3);
p_in_0 = p_batt_in_0 + p_sc_in_0 + p_pv_0;
p_lost_0 = p_batt_lost_0 + p_sc_lost_0;
p_out_0 = p_batt_out_0 + p_sc_out_0 + p_pv_0;
E_in_0 = E_batt_in_0 + E_sc_in_0 + E_pv_0;
E_lost_0 = E_batt_lost_0 + E_sc_lost_0;
E_out_0 = E_batt_out_0 + E_sc_out_0 + E_pv_0;
eff_0 = (1 - p_lost_0./(abs(p_batt_in_0) + abs(p_sc_in_0)))
* 100;
%%
% generates data for simulation with BATTERIES AND
SUPERCAPACITORS
sc_connection_status = 1;
```

```
sim('islanded_model_24hr')
v_batt_1 = data_batt(:,1);
i_batt_1 = data_batt(:,2);
p_batt_in_1 = data_batt(:,3);
p_batt_lost_1 = data_batt(:,4);
p_batt_out_1 = data_batt(:,5);
SOC_batt_1 = data_batt(:,6);
E_batt_in_1 = data_batt(:,7);
E_batt_lost_1 = data_batt(:,8);
E_batt_out_1 = data_batt(:,9);
v_sc_1 = data_sc(:,1);
i_sc_1 = data_sc(:,2);
p_sc_in_1 = data_sc(:,3);
p_sc_lost_1 = data_sc(:,4);
p_sc_out_1 = data_sc(:,5);
SOC_sc_1 = data_sc(:,6);
E_sc_in_1 = data_sc(:,7);
E_sc_lost_1 = data_sc(:,8);
E_sc_out_1 = data_sc(:,9);
v_load_1 = data_load(:,1);
i_load_1 = data_load(:,2);
p_load_1 = data_load(:,3);
i_pv_1 = data_pv(:,1);
p_pv_1 = data_pv(:,2);
E_pv_1 = data_pv(:,3);
p_in_1 = p_batt_in_1 + p_sc_in_1 + p_pv_1;
p_lost_1 = p_batt_lost_1 + p_sc_lost_1;
p_out_1 = p_batt_out_1 + p_sc_out_1 + p_pv_1;
E_in_1 = E_batt_in_1 + E_sc_in_1 + E_pv_1;
E_lost_1 = E_batt_lost_1 + E_sc_lost_1;
E_out_1 = E_batt_out_1 + E_sc_out_1 + E_pv_1;
eff_1 = (1 - p_lost_1./(abs(p_batt_in_1) + abs(p_sc_in_1)))
* 100;
time = time/3600;
%% SCs Disconnected
figure
subplot(2,1,1)
plot(time,p_in_0/1000,time,p_out_0/1000)
% title('Power Totals (SCs disconnected)')
xlabel('Time (hours)')
ylabel('Power (kW)')
legend('Total Input Power','Total Output Power')
axis([0 24 -inf inf])
xticks([0 4 8 12 16 20 24])
subplot(2,1,2)
plot(time,p_lost_0)
```

```
legend('Total Resistive Losses')
xlabel('Time (hours)')
ylabel('Power (W)')
axis([0 24 -inf inf])
xticks([0 4 8 12 16 20 24])
%% SCs Connected
figure
subplot(2,1,1)
plot(time,p_in_1/1000,time,p_out_1/1000)
% title('Power Totals (SCs connected)')
xlabel('Time (hours)')
ylabel('Power (kW)')
legend('Total Input Power','Total Output Power')
axis([0 24 -inf inf])
xticks([0 4 8 12 16 20 24])
subplot(2,1,2)
plot(time,p_lost_1)
legend('Total Resistive Losses')
xlabel('Time (hours)')
ylabel('Power (W)')
axis([0 24 -inf inf])
xticks([0 4 8 12 16 20 24])
figure
plot(time,i_batt_1,time,i_sc_1)
xlabel('Time (hours)')
ylabel('Current (A)')
legend('Battery Current','SC Current')
% title('Battery and SC Current (SCs connected)')
axis([0 24 -inf inf])
xticks([0 4 8 12 16 20 24])
figure
plot(time,SOC_batt_1,time,SOC_sc_1)
xlabel('Time (hours)')
ylabel('SOC (%)')
legend('Battery','SC')
% title('Battery and SC SOC (SCs connected)')
axis([0 24 -inf inf])
xticks([0 4 8 12 16 20 24])
%% Comparison between SCs connected and SCs disconnected
figure
plot(time,i_batt_0,time,i_batt_1)
xlabel('Time (hours)')
ylabel('Battery Current (A)')
legend('Batteries only','Batteries + SCs')
% title('Battery Current (SCs disconnected vs SCs
connected)')
```

```
axis([0 24 -inf inf])
xticks([0 4 8 12 16 20 24])
figure
plot(time,SOC_batt_0,time,SOC_batt_1)
xlabel('Time (hours)')
ylabel('Battery SOC (%)')
legend('Batteries only','Batteries + SCs')
% title('Battery SOC (SCs disconnected vs SCs connected)')
axis([0 24 -inf inf])
xticks([0 4 8 12 16 20 24])
figure
plot(time,E_lost_0/3600,time,E_lost_1/3600)
xlabel('Time (hours)')
ylabel('Resistive Losses (Wh)')
legend('Batteries only','Batteries + SCs')
% title('Resistive Losses (SCs disconnected vs SCs
connected)')
axis([0 24 -inf inf])
xticks([0 4 8 12 16 20 24])
%% PV Power Profile
figure
plot(time,p_pv_0/1000)
xlabel('Time (s)')
ylabel('Power (kW)')
% title('PV Panel Power')
axis([0 24 -0.1 3.1])
xticks([0 4 8 12 16 20 24])
```

```
% grid_connected_parameters_24hr.m
% Sets parameters for grid-connected DC microgrid
simulation
% time parameters:
tstep = 0.1;
tstop = 86400; % 10 hours for now, will be 24 hours later
% battery parameters:
N_Bs = 15;
N_Bp = 28;
R_B = 16e-3*10; % ohms
SOC_Bmax = 12; % A hr
SOC_B0 = SOC_Bmax; % A hr
SOC_B_data_vector = (0:100); % percent
v_Bimax = 12.86; % V (for each series element)
v_Bi_data_vector = 11.5:0.0136:v_Bimax; % V
i_Bmax = 40; % A (for each parallel branch)
% sc parameters:
N_SCs = 3;
N_SCp = 16;
R_esr = 8.1e-3; % ohms
SOC_SCmax = 57; % W hr
SOC_SC0 = SOC_SCmax; % W hr
C_sc = 130; % F
v_SCimax = sqrt(2*SOC_SCmax*3600/C_sc); % V (for each
series element)
i_SCmax = 1900; % A (for each parallel branch)
% filter parameters:
tau_lpf = 120;
fc_lpf = 1/(2*pi*tau_lpf);
tau_hpf = 120;
fc_hpf = 1/(2*pi*tau_hpf);
K_hpf = 25;
Kp_v = 0.5;
Ki_v = 0.1;
% bus voltage parameters
C_bus = 0.5;
v_bus_ref = 200;
% load parameters
load('Load')
R_load_inv = P_load/v_bus_ref^2;
% PV panel parameters
load('PV')
tau_pv = 120;
% generator parameters
load('Gen')
tau_gen = 120;
```

```
% grid_connected_script_24hr.m
% Simulates grid-connected DC microgrid model over 24 hours
% for SCs disconnected and SCs connected
% Generates Figures 27, 30-37
clear all
close all
clc
% generates data for simulation with BATTERIES ONLY
sc_connection_status = 0;
sim('grid_connected_model_24hr')
v_batt_0 = data_batt(:,1);
i_batt_0 = data_batt(:,2);
p_batt_in_0 = data_batt(:,3);
p_batt_lost_0 = data_batt(:,4);
p_batt_out_0 = data_batt(:,5);
SOC_batt_0 = data_batt(:,6);
E_batt_in_0 = data_batt(:,7);
E_batt_lost_0 = data_batt(:,8);
E_batt_out_0 = data_batt(:,9);
v_sc_0 = data_sc(:,1);
i_sc_0 = data_sc(:,2);
p_sc_in_0 = data_sc(:,3);
p_sc_lost_0 = data_sc(:,4);
p_sc_out_0 = data_sc(:,5);
SOC_sc_0 = data_sc(:,6);
E_sc_in_0 = data_sc(:,7);
E_sc_lost_0 = data_sc(:,8);
E_sc_out_0 = data_sc(:,9);
v_load_0 = data_load(:,1);
i_load_0 = data_load(:,2);
p_load_0 = data_load(:,3);
i_pv_0 = data_pv(:,1);
p_pv_0 = data_pv(:,2);
E_pv_0 = data_pv(:,3);
i_gen_0 = data_gen(:,1);
p_gen_0 = data_gen(:,2);
E_gen_0 = data_gen(:,3);
p_in_0 = p_batt_in_0 + p_sc_in_0 + p_pv_0 + p_gen_0;
p_lost_0 = p_batt_lost_0 + p_sc_lost_0;
p_out_0 = p_batt_out_0 + p_sc_out_0 + p_pv_0 + p_gen_0;
E_in_0 = E_batt_in_0 + E_sc_in_0 + E_pv_0 + E_gen_0;
E_lost_0 = E_batt_lost_0 + E_sc_lost_0;
E_out_0 = E_batt_out_0 + E_sc_out_0 + E_pv_0 + E_gen_0;
eff_0 = (1 - p_lost_0./(abs(p_batt_in_0) + abs(p_sc_in_0)))
* 100;
%%
```

```
% generates data for simulation with BATTERIES AND
SUPERCAPACITORS
sc_connection_status = 1;
sim('grid_connected_model_24hr')
v_batt_1 = data_batt(:,1);
i_batt_1 = data_batt(:,2);
p_batt_in_1 = data_batt(:,3);
p_batt_lost_1 = data_batt(:,4);
p_batt_out_1 = data_batt(:,5);
SOC_batt_1 = data_batt(:,6);
E_batt_in_1 = data_batt(:,7);
E_batt_lost_1 = data_batt(:,8);
E_batt_out_1 = data_batt(:,9);
v_sc_1 = data_sc(:,1);
i_sc_1 = data_sc(:,2);
p_sc_in_1 = data_sc(:,3);
p_sc_lost_1 = data_sc(:,4);
p_sc_out_1 = data_sc(:,5);
SOC_sc_1 = data_sc(:,6);
E_sc_in_1 = data_sc(:,7);
E_sc_lost_1 = data_sc(:,8);
E_sc_out_1 = data_sc(:,9);
v_load_1 = data_load(:,1);
i_load_1 = data_load(:,2);
p_load_1 = data_load(:,3);
i_pv_1 = data_pv(:,1);
p_pv_1 = data_pv(:,2);
E_pv_1 = data_pv(:,3);
i_gen_1 = data_gen(:,1);
p_gen_1 = data_gen(:,2);
E_gen_1 = data_gen(:,3);
p_in_1 = p_batt_in_1 + p_sc_in_1 + p_pv_1 + p_gen_1;
p_lost_1 = p_batt_lost_1 + p_sc_lost_1;
p_out_1 = p_batt_out_1 + p_sc_out_1 + p_pv_1 + p_gen_1;
E_in_1 = E_batt_in_1 + E_sc_in_1 + E_pv_1 + E_gen_1;
E_lost_1 = E_batt_lost_1 + E_sc_lost_1;
E_out_1 = E_batt_out_1 + E_sc_out_1 + E_pv_1 + E_gen_1;
eff_1 = (1 - p_lost_1./(abs(p_batt_in_1) + abs(p_sc_in_1)))
* 100;
time = time/3600;
%% SCs Disconnected
figure
subplot(2,1,1)
plot(time,p_in_0/1000,time,p_out_0/1000)
% title('Power Totals (SCs disconnected)')
xlabel('Time (hours)')
```

```
ylabel('Power (kW)')
legend('Total Input Power','Total Output Power')
axis([0 24 -inf inf])
xticks([0 4 8 12 16 20 24])
subplot(2,1,2)
plot(time,p_lost_0)
legend('Total Resistive Losses')
xlabel('Time (hours)')
ylabel('Power (W)')
axis([0 24 -inf inf])
xticks([0 4 8 12 16 20 24])
%% SCs Connected
figure
subplot(2,1,1)
plot(time,p_in_1/1000,time,p_out_1/1000)
% title('Power Totals (SCs connected)')
xlabel('Time (hours)')
ylabel('Power (kW)')
legend('Total Input Power','Total Output Power')
axis([0 24 -inf inf])
xticks([0 4 8 12 16 20 24])
subplot(2,1,2)
plot(time,p_lost_1)
legend('Total Resistive Losses')
xlabel('Time (hours)')
ylabel('Power (W)')
axis([0 24 -inf inf])
xticks([0 4 8 12 16 20 24])
figure
plot(time,i_batt_1,time,i_sc_1)
xlabel('Time (hours)')
ylabel('Current (A)')
legend('Battery Current','SC Current')
% title('Battery and SC Current (SCs connected)')
axis([0 24 -inf inf])
xticks([0 4 8 12 16 20 24])
figure
plot(time,SOC_batt_1,time,SOC_sc_1)
xlabel('Time (hours)')
ylabel('SOC (%)')
legend('Battery','SC')
% title('Battery and SC SOC (SCs connected)')
axis([0 24 -inf inf])
xticks([0 4 8 12 16 20 24])
%% Comparison between SCs connected and SCs disconnected
figure
```

```
plot(time,i_batt_0,time,i_batt_1)
xlabel('Time (hours)')
ylabel('Battery Current (A)')
legend('Batteries only','Batteries + SCs')
% title('Battery Current (SCs disconnected vs SCs
connected)')
axis([0 24 -inf inf])
xticks([0 4 8 12 16 20 24])
figure
plot(time,SOC_batt_0,time,SOC_batt_1)
xlabel('Time (hours)')
ylabel('Battery SOC (%)')
legend('Batteries only','Batteries + SCs')
% title('Battery SOC (SCs disconnected vs SCs connected)')
axis([0 24 -inf inf])
xticks([0 4 8 12 16 20 24])
figure
plot(time,E_lost_0/3600,time,E_lost_1/3600)
xlabel('Time (hours)')
ylabel('Resistive Losses (Wh)')
legend('Batteries only','Batteries + SCs')
% title('Resistive Losses (SCs disconnected vs SCs
connected)')
axis([0 24 -inf inf])
xticks([0 4 8 12 16 20 24])
%% PV and Generator Power Profiles
figure
plot(time,p_pv_0/1000)
xlabel('Time (s)')
ylabel('Power (kW)')
% title('PV Panel Power')
axis([0 24 -0.1 3.1])
xticks([0 4 8 12 16 20 24])
figure
plot(time,p_gen_0/1000)
xlabel('Time (s)')
ylabel('Power (kW)')
% title('Generator Power')
axis([0 24 -0.1 5.1])
xticks([0 4 8 12 16 20 24])
```

LIST OF REFERENCES

[1] "Navy Shore Energy Program," Commander, Navy Installations Command. Accessed December 4, 2017. [Online]. Available: https://www.cnic.navy.mil/om/base_support/facility_system_investment/Navy_Shore_Energy_Program.html

[2] "Energy," U.S. Navy Energy, Environment, and Climate Change. Accessed December 4, 2017. [Online]. Available: http://greenfleet.dodlive.mil/energy/

[3] *Shore Energy Management*, OPNAV Instruction 4100.5E, Chief of Naval Operations, Washington, DC, USA, 2012. [Online]. Available: http://greenfleet.dodlive.mil/files/ 2012/07/OPNAVINST-4100.5E.pdf

[4] B. Kroposki, T. Basso, and R. DeBlasio, "Microgrid standards and technologies," in *IEEE Power and Energy Soc. Gen. Mtg.—Conversion and Delivery of Electrical Energy in the 21st Century*, Pittsburgh, PA, 2008, pp. 1–4.

[5] G. Oriti, A. L. Julian, and N. J. Peck, "Power-Electronics-Based Energy Management System with Storage," *IEEE Trans. Power Electron.*, vol. 31, no. 1, pp. 452–460, Jan. 2016.

[6] J. M. Blanes, R. Gutiérrez, A. Garrigós, J. L. Lizán, and J. M. Cuadrado, "Electric vehicle battery life extension using ultracapacitors and an FPGA controlled interleaved buck-boost converter," *IEEE Trans. Power Electron.*, vol. 28, no. 12, pp. 5940–5948, Dec. 2013.

[7] B. Hredzak, V. G. Agelidis, and M. Jang, "A model predictive control system for a hybrid battery-ultracapacitor power source," *IEEE Trans. Power Electron.*, vol. 29, no. 3, pp. 1469–1479, Mar. 2014.

[8] H. Zhou, T. Bhattacharya, D. Tran, T. S. T. Siew, and A. M. Khambadkone, "Composite energy storage system involving battery and ultracapacitor with dynamic energy management in microgrid applications," *IEEE Trans. Power Electron.*, vol. 26, no. 3, pp. 923–930, Mar. 2011.

[9] A. M. van Voorden, L. M. Ramirez Elizondo, G. C. Paap, J. Verboomen, and L. van der Sluis, "The application of super capacitors to relieve battery-storage systems in autonomous renewable energy systems," in *IEEE Power. Tech.*, Lausanne, Switzerland, 2007, pp. 479–484.

[10] A. M. Gee, F. V. P. Robinson, and R. W. Dunn, "Analysis of battery lifetime extension in a small-scale wind-energy system using supercapacitors," *IEEE Trans. Energy Convers.*, vol. 28, no. 1, pp 24–33, Mar. 2013.

[11] P. Toma, P. Dorin, E. Radu, and M. Daniel, “Sizing photovoltaic-wind smart microgrid with battery storage and grid connection,” in *IEEE Int. Conf. on Automation, Quality and Testing, Robotics*, Cluj-Napoca, Romania, 2014, pp. 1–5.

[12] U. Akram, M. Khalid, and S. Shafiq, “An innovative hybrid wind-solar and battery-supercapacitor microgrid system- Development and Optimization,” *IEEE Access*, vol. 5, pp. 25897–25912, Oct. 2017.

[13] S. K. Kollimalla, M. K. Mishra, and N. L. Narasamma, “Design and analysis of novel control strategy for battery and supercapacitor storage system,” *IEEE Trans. Sust. Energy*, vol. 5, no. 4, pp. 1137–1144, Oct. 2014.

[14] G. Oriti, A. L. Julian, N. Anglani, and G. D. Hernandez, “Novel hybrid energy storage control for a single phase energy management system in a remote islanded microgrid,” in *IEEE Energy Conversion Congr. & Expo.*, Cincinnati, OH, 2017, pp. 1552–1559.

[15] W. Jang, L. Zhang, H. Zhao, H. Huang, and R. Hu, “Research on power sharing strategy of hybrid energy storage system in photovoltaic power station based on multi-objective optimisation,” *IET Renewable Power Generation*, vol. 10, no. 5, pp. 575–583, Apr. 2016.

[16] Q. Ling and Y. Lu, “An integration of super capacitor storage research for improving low-voltage-tide-through in power grid with wind turbine,” in *Asia-Pacific Power and Energy Engineering Conf.*, Shanghai, China, 2012, pp. 1–4.

[17] R. Lu, C. Zhu, L. Tian, and Q. Wang, “Super-capacitor stacks management system with dynamic equalization techniques,” *IEEE Trans. Magn.*, vol. 43, no. 1, pp. 254–258, Jan. 2007.

[18] D. B. Wickramasinghe Abeywardana, B. Hredzak, V. G. Agelidis, “Battery-supercapacitor hybrid energy storage system with reduced low frequency input current ripple,” in *4th Int. Conf. Renewable Energy Research and Applications*, 2015, pp. 328–332.

[19] K. V. Vidyanandan and N. Senroy, “Frequency regulation in a wind-powered diesel microgrid using flywheels and fuel cells,” *IET Generation, Transmission & Distribution*, vol. 10, no. 3, pp. 780–788, Mar. 2016.

[20] J. Feng, W. Gongbao, F. Lijun, Y. Yaqiao, W. Ruitian, and X. Zhen, “Controller design of flywheel energy storage systems in microgrid,” in *17th Annual Int. Conf. on Electrical Machines and Systems*, 2014, pp. 2821–2826.

[21] R. Arghandeh, M. Pipattanasomporn, and S. Rahman, “Flywheel energy storage systems for ride-through applications in a facility microgrid,” *IEEE Trans. Smart Grid*, vol. 3, no. 4, pp. 1955–1962, Sep. 2012.

[22] O. A. Mohammed and C. Lashway, “Modeling and energy management of modern shipboard power systems,” in *IEEE Energy Conversion Cong. and Exp.*, Cincinnati, OH, 2017, pp. 1–129.

[23] H. Miyoshi, T. Takeda, K. Yukita, Y. Goto, K. Ichiyanagi, T. Ushirokawa, and K. Yuasa, “Study on suppressing variation of storage battery power in microgrid using flywheel,” in *IEEE Int. Telecommunications Energy Conf.*, Osaka, Japan, 2015, pp. 1-5.

[24] R. L. Kelly, G. Oriti, and A. L. Julian, “Reducing fuel consumption at a remote military base,” *IEEE Elect. Mag.*, vol. 1, no. 2, pp. 30-37, Dec. 2013.

[25] G. M. Masters, *Renewable and Efficient Electric Power Systems*. Hoboken, NJ, USA: John Wiley & Sons, 2004.

[26] G. D. Hernandez, “Removal of direct current link harmonic ripple in single-phase voltage source inverter systems using supercapacitors,” M.S. thesis, ECE Dept., NPS, Monterey, CA, USA, 2016. [Online]. Available: https://calhoun.nps.edu/handle/10945/50559

[27] EnerSys, *Genesis NP12-12FR*, US-NP12-12-01, 2002. [Print].

[28] Tamilarasan P., A. K. Mishra, and S. Ramaprabhu, “Graphene/ionic liquid binary electrode material for high performance supercapacitor,” in *Int. Conf. on Nanoscience, Technology and Societal Implications*, Bhubaneswar, India, 2011, pp. 1–5.

[29] Maxwell Technologies, *BMOD0130 P056 B03 56 V Supercapacitor Module*, 1017119.3, 2013. [Online]. Available: http://www.maxwell.com/images/documents/56vmodule_ds_1017119-3.pdf

[30] N. Anglani, G. Oriti, and M. Colombini, “Optimized energy management system to reduce fuel consumption in remote military microgrids,” *IEEE Trans. Industry Applications*, vol. 53, no. 6, pp. 5777–5785, Dec. 2017.

THIS PAGE INTENTIONALLY LEFT BLANK

INITIAL DISTRIBUTION LIST

1. Defense Technical Information Center
   Ft. Belvoir, Virginia

2. Dudley Knox Library
   Naval Postgraduate School
   Monterey, California